Department of Physics and Astronomy
University of Heidelberg

Bachelor Thesis in Physics
submitted by

Michele Piero Blago

born in Heidelberg (Germany)

2015

Track Parameter Resolution Study of a Pixel Only Detector for LHC Geometry and Future High Rate Experiments

This Bachelor Thesis has been carried out by
Michele Piero Blago

at the
Physikalisches Institut Heidelberg

under the supervision of
Prof. Dr. André Schöning

Abstract

Recent progress in pixel detector technology and in the HV-MAPS technology in particular make it feasible to construct an all-silicon pixel detector as a future alternative for large scale particle experiments like ATLAS or CMS. Previous studies have indicated that nine layers of pixel sensors, in comparison to the 14 detector layers planned for Inner Tracker ATLAS upgrade, are sufficient to reliably reconstruct particle trajectories. In this thesis the performance of a nine layer all-pixel detector is studied for different material thicknesses based on a full *Geant4* simulation.

Furthermore, the ability of an all-pixel detector to form trigger decisions using a special triplet pixel layer design is investigated. Such a design could be used to reconstruct all tracks originating from the proton-proton interaction at the first hardware level at 40 MHz collision frequency.

Zusammenfassung

Die Fortschritte der letzten Jahre in der Pixel- und insbesondere der HV-MAPS Technology ermöglichen die Realisierung eines Detektors der außschließlich Pixel-Sensoren verwendet, als eine zukünftige Alernative für Hochenergie-Experimente wie ATLAS oder CMS. Vorrangegangene Untersuchungen haben gezeigt, dass neun Detektorlagen, gegenüber den geplanten 14 des ATLAS Inner Tracker Upgrades ausreichen, um verlässlich Teilchenspuren zu rekonstruieren. In dieser Arbeit wird die Genauigkeit der Spurrekonstruktion eines außschließlich aus neun Pixellagen bestehenden Detektors für verschiedene Materialdicken in einer umfassenden *Geant4* Simulation untersucht.

Darüber hinaus wird die Möglichkeit eines solchen Pixeldetektors Triggerentscheidungen zu treffen erforscht. Hierfür wird ein spezielles Konzept von Pixel-Dreierlagen verwendet, das die volle Rekonstruktion der Spuren aus Proton-Proton Kollision von 40 MHz bereits auf der ersten Hardware Ebene ermöglicht .

Contents

Contents

1 Introduction

With the start of the Large Hadron Collider (LHC) in 2008 a new chapter in particle physics was launched. So far unreachable energy scales were made accessible to further investigate the fundamentals of the Standard Model and physics beyond. The detectors used in the experiments had to grow both in size and robustness to fit the new scale of the accelerator. Furthermore, each upgrade of the LHC centre of mass energy and luminosity such as in spring 2015 or around the year 2020 puts new challenges to the detectors.

The goal of experiments such as ATLAS, CMS or future high rate experiments at envisioned accelerators like the Future Circular Collider (FCC) is to to measure rare decay signatures in large background. Therefore, as much information as possible has to be collected from the particle collisions. That is on the one hand realised by very high luminosity and bunch crossing rate of the collided particles. On the other hand the information lies within the tracks resulting from the collisions and can only be obtained by precise reconstruction of their parameters. As a result, reconstruction performance has to be increased with rising energy and luminosity of a collider.

To achieve the adequate reconstruction performance, the detector design has to be in compliance with the experimental goals in terms of what is the experiment's purpose and what processes and parameters are to be studied. General purpose detectors as in the ATLAS or CMS experiment usually consist of a barrel shaped detector with so called endcaps. The endcaps are disc-shaped detecor layers which are orthogonally aligned to the beamline (see Figure 1.1). As an example, the design of the ATLAS inner pixel detector is shown in Figure 1.1. This detector features a hermetic design which allows nearly complete acceptance. That means that every particle should cross the three detector layers either in the barrel or the endcap region. In total, the ATLAS inner detector consists of three pixel detector layers and eight silicon-strip detector layers all positioned in a barrel shape around the beam axis. The endcap region is composed of three pixel detector discs and nine silicon strip discs.

A similar composition of barrel- and disc- detectorlayers on the second general purpose detector a the LHC, CMS can be observed. Here, the number of layers is even higher with 13 tracking layers of which three are pixel layers and the other ten are silicon strip detecor layers. The endcap region consist in total of 14 layers.

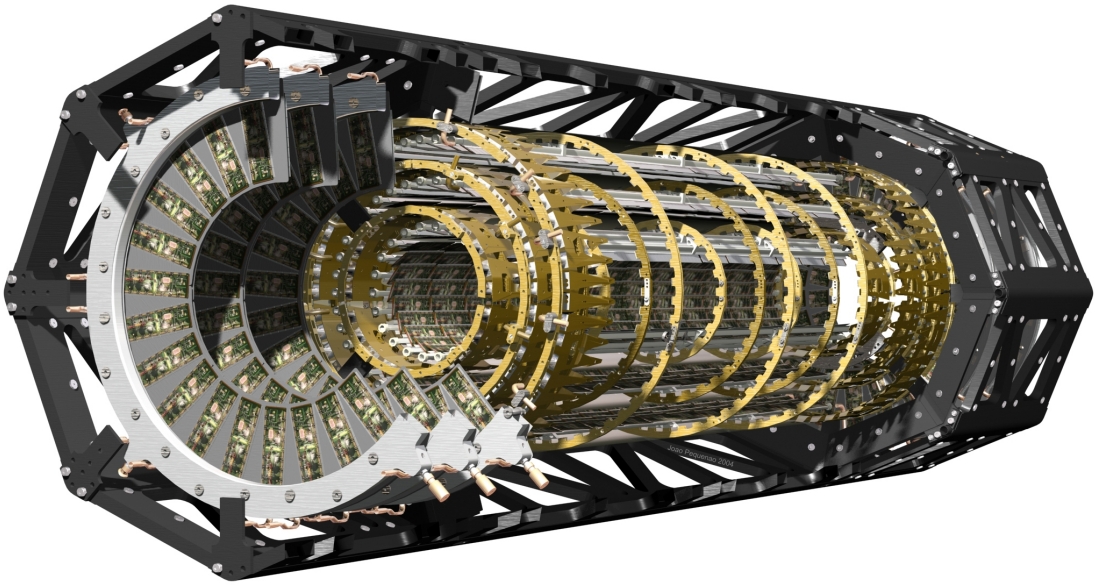

Figure 1.1: The ATLAS pixel detector consisting of three barrels at the radii 5cm, 9cm, 12cm and endcaps with innner radius of 9 and outer radius of 15 cm. Taken from [1]

In order to precisely reconstruct particle trajectories a large number and also a variety of detector techniques are used in those two examples. In the barrel region, both consist of pixel detectors close to the interaction point and are surrounded by strip detectors. Together with the disc detectors at the endcaps a hermetic set up is completed, which ensures that particles can not pass without being detected and leave enough information on their tracks to be reconstructed.

Having that said, the complex composition of the tracking systems increases the material budget, which causes energy loss and track deviation of particles, and it increases the power consumption of the detector.

1.1 Motivation

In contrast to the tracking detectors mentioned above which consist of both pixel- and strip-detectors this thesis investigates a new pixel-only detector design for the upcoming upgrade in 2020 with the perspective to enhance the reconstruction possibilities of LHC- or future high-rate experiments.

The motivation for using pixel detectors lies in the resulting simplicity of the detector design, since less layers are required for a pixel-only detector to achieve the same reconstruction results as for nowadays detector setups. Therefore, the material budget can

be reduced which is a key factor in particle experiments since particle should interact as little as possible with the detector itself. The progress of the pixel sensor technology and cooling systems over the last years allows to build detector layers with a relative radiation length in the order of magnitude of several permille. Even for a large scale and high-energy experiment such as ATLAS, CMS or experiments at the FCC relative radiation lengths of maximal 1% can be realised compared to 2% as the figure of merit for nowadays detectors at the LHC.

By time the detector presented in this thesis would find its earliest chance to be realised in an experiment, namely with the LHC upgrade around the year 2020, pixel-detector technology is not only likely to have matched this goal but to have excelled it. This places pixel detectors well ahead of strip detectors in terms of measurement precision and material budget. In order to take advantage of this progress it is crucial to not only rely on the usual layout of all purpose detectors which was described above but to go for detector designs less complex in structure with more pixel layers and thereby less total number of detector layers.

For that reason, this thesis studies the barrel region of a pixel-only detector consisting of only nine layers in total. Three thicknesses for the detector layers are investigated and compared: 0.1%, 1% and 2% of a radiation length. A full *Geant4* [2] simulation is used to determine the resolution of reconstructed track parameters. In addition, a trigger application of the proposed design is discussed.

2 Particle Interactions in Geant4

The computer simulation used in this thesis is based on the *Geant4* framework, which includes a large amount of particle interactions in realistically simulate an experiment [2]. The *Geant4* toolkit itself is using Monte Carlo methods to account for the statistical nature of particle features and interactions. It covers particle transport and decay, electromagnetic interactions, hadronic interactions, and gamma- and lepto-nuclear interactions in great detail. Therefore, in this section, the most relevant processes are discussed and remarks on their implementation into the simulation toolkit *Geant4* are given. This is necessary to account for since the simulation of particle interactions and their characteristics is often limited by the computing power. Thus simplification models are crucial in order to find the best compromise between an accurate description of interactions and an efficient simulation of the same. This overview of particle interactions is mainly based on the extensive documentation of *Geant4* (see [2] and [3]).

2.1 Minimum-Ionising Particles

In general, the energy which is lost when charged particles traverse matter is well described by the Bethe equation (2.1) with variation from the true value by a few percent ([3] Eq. 32.5).

$$\left\langle -\frac{\mathrm{d}E}{\mathrm{d}x} \right\rangle = K z^2 \frac{Z}{A} \frac{1}{\beta^2} \left[\frac{1}{2} \ln \frac{2 m_e c^2 \beta^2 \gamma^2 W_{max}}{I^2} - \beta^2 - \frac{\delta(\beta\gamma)}{2} \right]. \tag{2.1}$$

K ([3] Tab.32.1) combines the natural constants Avogadro Number N_A, electron mass m_e, speed of light c and the fine structure constant α as shown in (2.2). Moreover, the atomic number of the absorbing material is Z, its atomic mass is A and W_{max} describes the maximum energy transferred to an electron in one collision. γ is the Lorentz factor and $\beta = v/c$ the particle velocity in units of the speed of light c. The factor $\delta(\beta\gamma)/2$ is the density effect correction which is in more detail described in [3] and illustrated by a green line in Figure 2.1.

$$K = 4\pi N_A r_e^2 m_e c^2 / \alpha, \tag{2.2}$$

where r_e is the classical radius of the electron. Since, in our case, no heavy nuclei are passing through the detector, higher order terms accounting for photon coupling and the detector particles interaction size can be neglected.

The maximum amount of energy W_{max} ([3] Eq. 32.4) transferred by a particle in one collision is given by

$$W_{max} = \frac{2m_e c^2 \beta^2 \gamma^2}{1 + 2\gamma \frac{m_e}{M} + \left(\frac{m_e}{M}\right)^2}, \tag{2.3}$$

where M is the mass of the particle. In high-energy physics applications where particle energies go above $100\text{GeV}/c^2$ the momentum transferred to the shell electron of the material may be greater than $1\text{GeV}/c$ which introduces additional hadronic effects. Those are discussed later in 2.4.

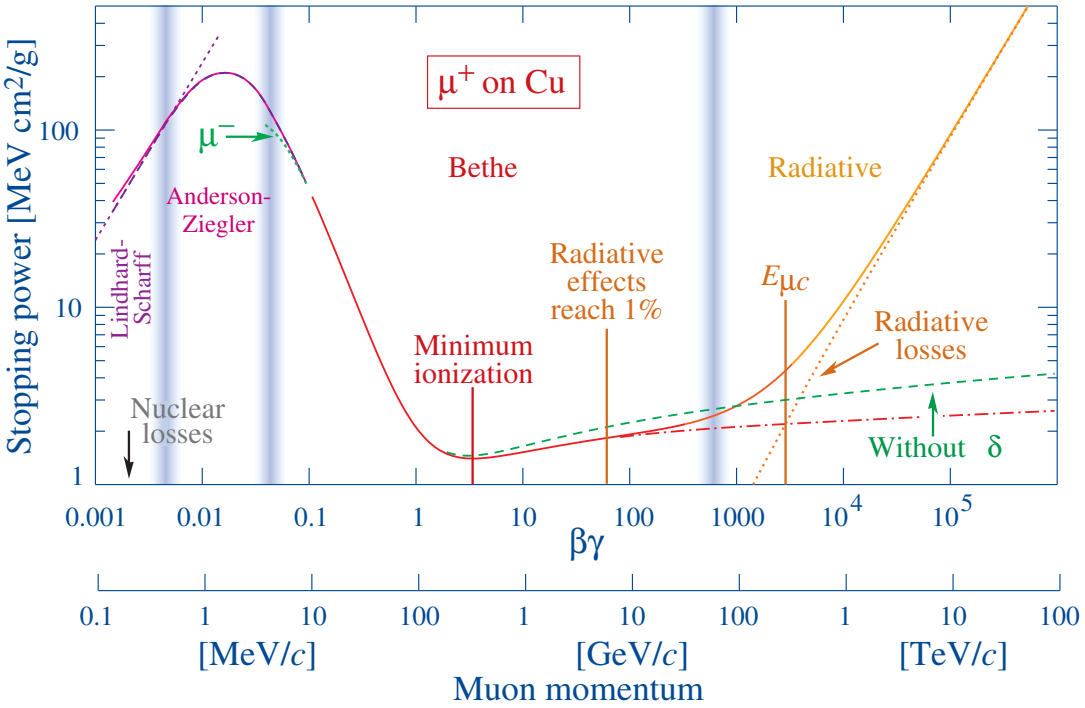

Figure 2.1: Stopping power for a positive muon in copper. Between the second and third vertical blue line the curve is described by the Bethe equation (2.1) .Taken from [3].

Figure 2.1 shows the stopping power $\left(= \left\langle -\frac{dE}{dx} \right\rangle \right)$ of a positive muon in copper. Equation (2.1) describes the function between the second and third vertical blue line. This energetic range is of particular interest in this context since it is valid for the vast majority of particles stemming from a *pp*-collision in the LHC. As one can see, the

stopping power features a broad minimum. Particles close to this minimum are so-called 'minimum-ionising particles' or short MIPs. Therefore, by studying the behaviour of MIPs in a particle detector, one can already characterise its most important features. Due to this fact, in this study, major interest lies in investigating the interaction of positive muons, electrons and pions with the detector material at an energy of $1\mathrm{GeV}/c^2$. Those three particles by good extent represent the large variety of particles from a collision and their interaction processes with the detector material.

2.2 Particle Decay

With the magnet in the simulated detector being closely located around the last detector layer (explained in more detail in Chapter 3) recurling particles are unlikely since their trajectory straightens after leaving the homogeneous magnetic field. Consequently, the decay of primary particles is a minor factor regarding background. Having said that, particles with less momenta are often created by interaction of primaries with the detector material. Those particles *do* recurl inside the detector, which makes an overview over the decay modes implemented necessary. The *Geant4* simulation accounts for the decay of a particle using its velocity at the time of its creation ([2] Chapt. 4.1). Hence, the mean free path λ of the particle is given by

$$\lambda = \gamma\beta c\tau, \tag{2.4}$$

depending on the particles lifetime τ. Using β, the time after which the particle decays in its rest frame is then translated into its decay length. With regard to the branching ratio of the particle, the resulting secondary particles and their kinematic behaviour is determined depending on its decay mode.

The most relevant decay modes in this context are *phase space decay* and *muon decay*. In general, the phase space decay mode comprises the two-, three- or many-body decays such as

$$\pi^+ \to \mu^+\nu_\mu, \tag{2.5}$$

or

$$\pi^+ \to \pi^0 e^+\nu^+, \tag{2.6}$$

where the angles under which the secondary particles spread are isotropic in the centre-of-mass system of the original particle.

The muon decays in its usual form, the Michel decay. For the μ^+, the dominant decay mode is

$$\mu^+ \rightarrow e^+ \nu_e \bar{\nu}_\mu. \tag{2.7}$$

The amount of energy transferred to the electron is determined by (2.8) ([2] Chapt. 4.1) using the electron energy E_e and its maximum energy, depending on the muon mass E_μ, $E_{max} = m_\mu/2$ as a variable of the differential decay rate $\mathrm{d}\Gamma$ ([2] Chapt. 4.2.3):

$$\mathrm{d}\Gamma = \frac{G_F^2 m_\mu^5}{192\pi^3} 2 \left(\frac{E_e}{E_{max}} \right)^2 \left(3 - 2\frac{E_e}{E_{max}} \right), \tag{2.8}$$

with the Fermi coupling constant G_F. Again, the fact is stressed that the great majority of particles produced in a collision does not decay inside the detector as their relativistic velocities leads to much longer lifetimes in the laboratory system.

2.3 Electromagnetic Interactions

In contrast to particle decays, electromagnetic effects are a major contribution to background and additionally cause deviations from the undisturbed particle trajectory. Consequently, on the one hand, one has to account interactions resulting in the production of secondary particles while crossing the material and on the other hand the effect the material has on the path of a particle depending on its nature and energy.

2.3.1 Gamma Interactions

In high-energy experiments such as proton-proton collisions at the LHC, a large amount of photons with a wide range in energy is produced. This leads in many cases to the production of charged particles, thus, adding to the background in most detector applications. In order to take into account this background, the underlying processes have to be understood. In the following, the most important interactions are discussed.

Photoelectric Effect

The photoelectric effect describes the emission of an electron as a result of the deposition of the photon energy in the material. This is the case if the energy of the photon E_γ is larger than the binding energy of the atomic shell $B_{shell}(Z)$ depending on the atomic number Z of the absorbing material. The difference is consequently carried away by the electron in form of kinetic energy $T_{el} = E_\gamma - B_{shell}(Z)$.

Compton Scattering

Another scenario where an electron is emitted due to a photon is inelastic scattering of the latter by the shell electrons of the atoms. The kinetic energy of the electron T_{el} is in this case determined by the energy difference of the incoming photon $E_{\gamma,in}$ to the scattered photon $E_{\gamma,out}$. Therefore, $T_{el} = E_{\gamma,in} - E_{\gamma,out}$ depends on the scattering angle θ of the photon which is defined by the Compton equation ([2] Eq. 5.8):

$$E_{\gamma,out} = E_{\gamma,in} \frac{m_e c^2}{m_e c^2 + E_{\gamma,in}(1 - \cos\theta)}. \tag{2.9}$$

Gamma Conversion

When a photon traverses a material with i elements and n_i atoms in this element, its mean free path to produce a pair of e^+ and e^- is determined by ([2] Eq. 5.16)

$$\lambda(E_\gamma) = \Big(\sum_i n_i \cdot \sigma(Z_i, E_\gamma) \Big)^{-1}, \tag{2.10}$$

with the cross section $\sigma(Z_i, E_\gamma)$ for the conversion. The cross section implementation in *Geant4* varies as indicated for the arguments Z_i and E_γ in the case of $E_\gamma \in [1.5\text{MeV}, 100\text{GeV}]$ and is constant above this range. In case the pair production,originally investigated by Bethe and Heitler [4], is occurring due to interaction with a nucleus of mass M, this conversion requires

$$E_\gamma \geq 2 m_e c^2 \Big(1 + \frac{m_e}{M}\Big), \tag{2.11}$$

in order to provide at least the energy for the electron and positron at restmass.

Analogously, the photon can convert into a $\mu^+\mu^-$-pair when interacting with the detector material's nuclei or shell electrons. In this process, the entire photon energy is transferred to the muons such that $x_+ + x_- = 1$ for the two energy fractions $x_+ = E_\mu^+ / E_\gamma$ and $x_- = E_\mu^- / E_\gamma$. The differential cross section in this case is ([2] Eq. 5.39)

$$\frac{\mathrm{d}\sigma}{\mathrm{d}x_+} = 4\alpha Z^2 r_\mu^2 \Big(1 - \frac{4}{3} x_+ x_- \Big) \log(W), \tag{2.12}$$

with the nucleus charge Z, classical muon radius r_μ and a constant of the interaction material W. The cross section is positive for $E_\gamma > 4m_\mu$ and is otherwise set to zero by Geant.

2.3.2 Multiple Scattering and its Simulation in *Geant4*

The trajectory of a particle is disturbed due to scattering processes with nuclei and electrons. Since the most relevant deviations stem from crossings of material of non-gaseous density, the main remark lies not on single scattering processes but on the statistical effect of many of those single interactions. The main contributor is Coulomb scattering of the particle with nuclei of the traversed material which is characterised by the Rutherford cross section [5],

$$\frac{\mathrm{d}\sigma}{\mathrm{d}\Omega} = \left(\frac{1}{4\pi\epsilon_0}\frac{Z_1 Z_2 e^2}{4E_{in}}\right)^2 \frac{1}{\sin^4(\frac{\theta_R}{2})}, \tag{2.13}$$

describing the probability for the particle to be scattered into the solid angle $\mathrm{d}\Omega$ after being deviated by θ_R. Here, ϵ_0 is the electric constant, E_{in} the initial energy of the particle, and Z_1, Z_2 are the atomic number for the particle and the scattering material, respectively. For hadronic particles also strong interactions result in deviations. The distribution of the multiple scattering angle θ_{MS} is nearly gaussian, with zero mean value but with symmetric tails on both sides.

In order to create a joint distribution of θ_{MS} in a Monte Carlo simulation one can either take each single scattering into account, which results in a precise but very expensive result in terms of computing time. The other option is to simulate global parameters for energy loss, displacement and deviation of the particle in the so-called *condensed* simulation algorithm. A middle course between these two approaches is to treat the normally distributed so-called *soft* collisions with small deviations globally and the much less frequent *hard* scattering individually. In *Geant4*, however, the global solution is used.

In a computer simulation, a particle and its interactions with the simulated world is, unlike the real world case, divided in discrete steps. After each step, the incidents that happened depending on the crossed volume are updated and with them the effects on the particle itself, whether it decays, is scattered, displaced, etc. Furthermore, one needs to distinguish between the *geometrical path length* z, which is the length of the bent path of the particle in a magnetic field, and a straight line in the absence of a magnetic field. The relation of the mean geometrical path length to the *true path length* of the particle t is described by ([2] Eq. 6.2)

$$\langle z \rangle = \lambda_1 \left[1 - \exp\left(-\frac{t}{\lambda_1}\right)\right], \tag{2.14}$$

where λ_1 is the first *transport mean path*. The transport mean path determines the individual features of the particle's multiple scattering. Its k-th element in a volume with n_a atoms is defined as ([2] Eq. 6.1):

$$\frac{1}{\lambda_k} = 2\pi n_a \int_{-1}^{1} [1 - P_k(\cos\chi)] \frac{\mathrm{d}(\chi)}{\mathrm{d}\Omega} \mathrm{d}(\cos\chi), \tag{2.15}$$

with the k-th Legendre polynomial $P_k(\cos\chi)$. The underlying mathematical principles used by *Geant4* are based on the original descriptions of multiple scattering in [6] and [7]. The mean value of $\cos(\theta_{MS})$ and its variance σ_{MS} after a step t is then given by ([2] Eq. 6.3, 6.4)

$$\langle \cos\theta_{MS} \rangle = \exp\left[-\frac{t}{\lambda_1} \right], \tag{2.16}$$

$$\sigma^2_{MS} = \langle \cos^2\theta \rangle - \langle \cos\theta \rangle^2 = \frac{1 + 2e^{-2\kappa\tau}}{3} - e^{-2\tau}, \tag{2.17}$$

with $\tau - t/\lambda_1$ and $\kappa = \lambda_1/\lambda_2$.

For most cases, it is sufficient only to use the projected angle distribution θ_0 with its gaussian approximation, hence neglecting the tails of the distribution. In this case the projected angle is given by the Highland-Lynch-Dahl equation [8] [9]:

$$\theta_0 = \frac{13.6\mathrm{MeV}}{\beta cp} Z \sqrt{\frac{x}{X_0}} \left[1 + h_c \ln\left(\frac{x}{X_0} \right) \right], \tag{2.18}$$

where Z is the charge number of the projectile, $\frac{x}{X_0}$ the path length in units of radiation length of the particle (in case of the simulation $x = t$, the true path length) and the correction factor $h_c = 0.038$.

2.3.3 Energy Losses of $e^{\pm}$

The interaction processes of electrons and positrons are unlike those of heavier particles. This is due to the large discrepancy that heavy particles have towards the electrons they ionise whereas the electrons itself are naturally similar in terms of spin and mass to their ionising opponent. To account for this distinct collision behaviour, the case of the electron (positron) is discussed in section 2.1.

As one can see in Figure 2.2 the relative fractional energy loss by an electron is divided into several different scattering processes depending on its energy. In our energy range the Møller and Bhabha scattering for low energy electrons and positrons is not explained in detail. Of special importance is bremsstrahlung which is the major cause of $e^{\pm}$ energy loss in high-energy epxeriments.

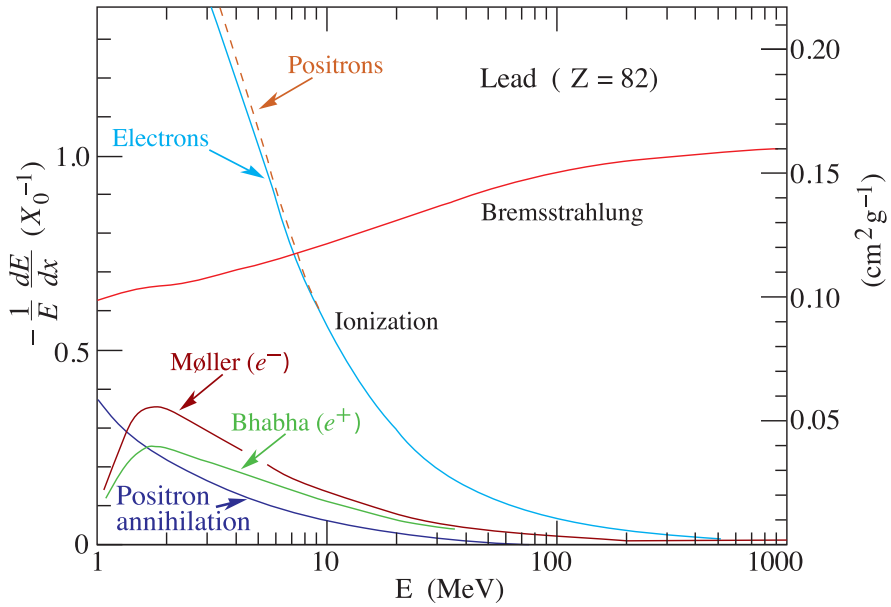

Figure 2.2: Energy loss by an electron or positron traversing lead for varying energies. Taken from [3].

Stopping Power of $e^{\pm}$

Since scattering and projectile particle are of the same type the maximum energy transfer W_{max} from equation (2.3) is modified to

$$W_{max} = \frac{1}{2} m_e c^2 (\gamma - 1), \tag{2.19}$$

in case of single electron-electron scattering. The factor $\frac{1}{2}$ accounts the identity of the two interacting particles. Hence, in case of electron-positron scattering this factor is missing in the maximum energy transfer Equation (2.19). As mentioned, our energy regime diminishes the effects of $e^{\pm}$ energy loss due to collision transfers. Because of the fact that even in low energy regimes the effects for electrons and positrons do only differ slightly, there is no need to pay extra attention to distinguish those two. As illustrated in Figure 2.2 positron annihilation effects are also negligible above 100MeV.

Bremsstrahlung

As previously stated, the energy loss due to bremsstrahlung is the major component for electrons and positrons in this context. In the case of bremsstrahlung, the energy lost by a charged particle, here an electron or positron, due deflection from its undisturbed path is discarded by emitted photons. This deflection is caused by the interaction with

the electromagnetic field of an atom. The cross section for this process is determined in the approximation given by Tsai ([10], Eq.3.9):

$$\frac{\mathrm{d}\sigma}{\mathrm{d}k} = \frac{1}{k} 4\alpha r_e^2 \left\{ \left(\frac{4}{3} - \frac{4}{3}y + y^2 \right) \left[Z^2 (L_{rad} - f(Z)) + Z L'_{rad} \right] + \frac{1}{9}(1-y)(Z^2+Z) \right\}. \quad (2.20)$$

Here, the percentage of the energy transferred from electron to photon is $y = k/E$, where E is the electron energy and k the Bremsstrahlung photon energy. This approximation is referred to as the *complete screening case*. Moreover, the function $f(Z)$ given in this context can be well approximated from its original infinite sum by ([3] Eq. 32.27)

$$f(Z) = a^2 \left[(1+a^2)^{-1} + 0.20206 - 0.0369a^2 + 0.0083a^4 - 0.002a^6 \right]. \quad (2.21)$$

The factors L_{rad} and L'_{rad} are material dependent constants and can be found for a selection of elements used in this simulation in Table 2.1. Using Tsai's complete screening approximation the number of photons N_γ with energy $k \in [k_{min}, k_{max}]$ can be calculated using ([3] Eq. 32.31)

$$N_\gamma = \frac{d}{X_0} \left[\frac{4}{3} \ln\left(\frac{k_{max}}{k_{min}} \right) - \frac{4(k_{max} - k_{min})}{3E} + \frac{k_{max}^2 - k_{min}^2}{2E^2} \right], \quad (2.22)$$

if the traveled distance d is much smaller than the radiation length X_0, which is further discussed in the following section.

Radiation Length

The radiation length characterises the penetration features of a material. It corresponds not only to 7/9 of the mean free path for pair production considering a photon of high energy as discussed in Section 2.3.1 but also to the distance for which an electron's energy decreases by a factor of $1/e$. This is only valid for energies above the critical energy. However, as mentioned before, we are well above the critical energy, which is of the order of magnitude 10MeV.

For the radiation length X_0 we are again using the definition of Tsai ([10], Eq.3.66):

$$\frac{1}{X_0} = 4\alpha r_e^2 \frac{N_A}{A} \left\{ Z^2 [L_{rad} - f(Z)] + Z L'_{rad} \right\}. \quad (2.23)$$

where $A = 1\mathrm{g/mol}$. The radiation length for some materials used in the simulated detector are illustrated in Table 2.1.

Table 2.1: For a selection of elements used in the detector the paramters L_{rad} and L'_{rad} used in Equation (2.20) and (2.23) are depicted together with the radiation length of the materials. Parameters taken from [3] and X_0 from [11]

Element	Z	L_{rad}	L'_{rad}	X_0[g/cm^2]
He	2	4.79	5.621	94.32
Be	4	4.71	5.924	65.19
Al	13	4.36	5.375	24.01
Si	14	4.34	5.326	21.82

In order to calculate the radiation length of a compound material an approximating solution can given by ([3] Eq. 32.28)

$$\frac{1}{X_0} = \sum_i \frac{\omega_i}{X_i}. \tag{2.24}$$

2.4 Hadronic Interactions

Investigating the collision of two protons is the main purpose of the Large Hadron Collider meaning that the interaction processes of hadrons are of high importance in LHC analysis. In this thesis, hadronic interactions are far from being dominant due to their short interaction length, which is explained in this chapter. However, they do occur, especially when simulating momenta up to 100 GeV/c, which is part of this study. Consequently, in the following section an overview of some of the most important hadronic processes is given. In particular the term interaction length will be illustrated as well as the possibility of secondary particles.

2.4.1 Hadronic Interaction Length

The high-energy range with particles of momenta 1GeV and above is the scope of high-rate and high-luminosity experiments and thus the scope which is investigated in this thesis. As a result, we can neglect the electrostatic repulsion that prevents interactions such as those of a proton with the equally charged nucleus. Furthermore, quantum effects do not have to be taken into account, since at those energies the particle's wavelength is small compared to the size of a nucleus. Therefore, an approximation for the nuclear mean free path can be given by ([12], Chap.2):

$$\lambda_{nuclear} = \frac{A}{\sigma_{in} N_A \rho}, \tag{2.25}$$

where A is the atomic number of the nucleus, N_A the Avogadro number and ρ the density of the material. σ_{in} denotes the cross section for inelastic hadronic interactions. This mean free path of a proton given in (2.25) is also called the hadronic interaction length. At the high energies which are examined in this context the range of the proton is most cases not limited by energy loss due to ionisation but by nuclear interactions. the consequences of this are explained in the next section.

2.4.2 Secondary Particles from Hadronic Interactions

The nuclear interactions result in the disruption of the nucleus which results in many collision products, the so called secondary particles. The main proportion of the secondaries is likely to be pions ([12], Chap.3.7) but also Kaons are produced. An exemplary reaction resulting in the production of a Kaon-Antikaon pair is

$$pp \rightarrow ppK^+K^-, \tag{2.26}$$

and a possible reaction leading to a secondary pion is for example given by

$$pp \rightarrow pp\pi^0. \tag{2.27}$$

One can see that in these interactions the protons involved loose some of their energy which allows the creation of a secondary particle. The explicit energetic requirements for the interactions to occur is not given here but it is emphasised that secondary particles are produced in hadronic interactions and hence produce a background signal.

3 Detector Realisation and Track Reconstruction

In this chapter first the pixel technology is discussed which makes the realisation of an all-pixel detector possible. Then the *triplet9* detector design is presented with respect to its simulation. In the end the track reconstruction and the methods used for this purpose are explained.

3.1 HV-MAPS

The recent progress in pixel technology is the groundwork for developing a pixel-only detector ready to be put into action in LHC or future high-rate experiments. One of the most promising candidates to fulfill these requirements is the High-Voltage Monolithic Active Pixel Sensor (HV-MAPS) which is planned to be used for the Mu3e experiment. An insight into the working principle is given in this section.

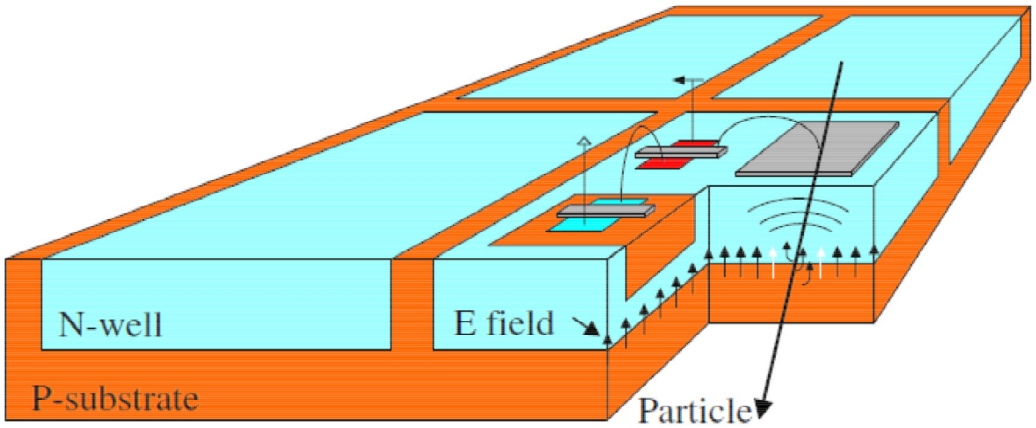

Figure 3.1: Functioning of the HV-MAPS detector design. Taken from ([13] Fig.10.1)
.

One of the two main advantages the HV-MAPS provides is to combine readout electronics and sensor into a single unit, thus greatly reducing the material budget and thereby the radiation length of a detector layer. This is in contrast to sensor designs

which need an readout extra chip and further bonding material, which is true for the so-called hybrid sensor designs. In the case of hybrid designs the sensor is bump-bonded to a read out chip (eg. CMOS). Therefore, in contrast to the HV-MAPS every part is placed individually and is not integrated but connected resulting in a high material budget.

Furthermore, a high bias voltage is applied. In the context of sensor technology this refers to 50 or more Volts. That results in charge collection via drift rather than diffusion as common in MAPS, hence greatly reducing timing resolution to less than 10 ns. Another great advantage of charge collection by drift rather then by "random walk" is the increase in radiation hardness which is of particular interest for the application in high-energy and high-rate experiments with the sensors close to the beamline. The increase in readiation hardness comes from the fact that for charge collection via diffusion the radiation damage creates "traps" for the charged particles in terms of an attractive potential. However, with an applied high voltage as for the HV-MAPS the particles can overcome the traps due to the higher attraction and are collected.

Figure 3.1 illustrates the principle of the design where one can see that the electronics for the amplifier is directly integrated into the deep N-well. Another feature of the sensor is zero suppression which reduces the amount of processed pixel information, meaning that only particle crossings produce a signal. The detectors can be produced with a thickness of only 50 μm due to the small depletion zone.

The pixel size used in this study is of $80\mu\text{m}\times80\mu\text{m}$. This will be important in the comparison of the two track reconstruction algorithms discussed in Chapter 3.3.2 and 3.3.3. It needs to be mentioned at this point that it possible to decrease the pixel size down to $40\times40\mu\text{m}$ which is not studied here[1] but will shift the weight of multiple scattering- and spatial hit-uncertainty in the track reconstruction.

What makes the HV-MAPS one of the main candidates for future pixel-detectors is their reasonably priced production, possible due to the industrial HV-CMOS processing which was jointly developed by AMS and IBM. Further information on the HV-MAPS and HV-CMOS can be found in the Mu3e research proposal [13] or [14], [15]. The latter studies the radiation hardness of the sensor with promising results for the implementation in LHC upgrades or other high-energy and high-luminosity experiments.

3.2 Detector Design and Simulation

This thesis investigates a pixel-only detector consisting of nine layers. The layers are arranged as three triple-layers, where a triple-layer designates three closely stacked individual layers. This design is based on a previous study [16] which showed promising

[1] The change of such a fundamental element in the simulation goes beyond the scope of a bachelorthesis.

results in terms of track reconstruction performance and the capability of the design to function as a track trigger with only the outermost triple-layer as a working unit. Additionally, this study compared the triple-layer design with the more standard double-layers and equidistant layer distributions both for the total number of six and nine layers with the result that the most suited candidate for a pixel-only detector in LHC and other high-rate experiments is given by the so called *triplet9* design that is presented here with emphasis on track reconstruction as its main advantage. The goal of this thesis is not to reproduce the results of this comparison but to test the functionality and capabilities of the *triplet9* design in a full *Geant4* [2] simulation. Hence, it accounts the particle interactions in great detail given by the high accuracy that *Geant4* embeds in the interaction processes of which some were described in Chapter 2. The simulation is based on the Mu3e-Framework [13] with a modified detector layout, event generation and track reconstruction.

3.2.1 Simulation

The simulated detector elements are from inside to outside the beampipe, the nine sensor ladders, and the magnet. The whole detector without the Magnet is illustrated in Figure 3.2. A transverse view of the entire setup is shown in Figure 3.4.The individual elements are described in the following.

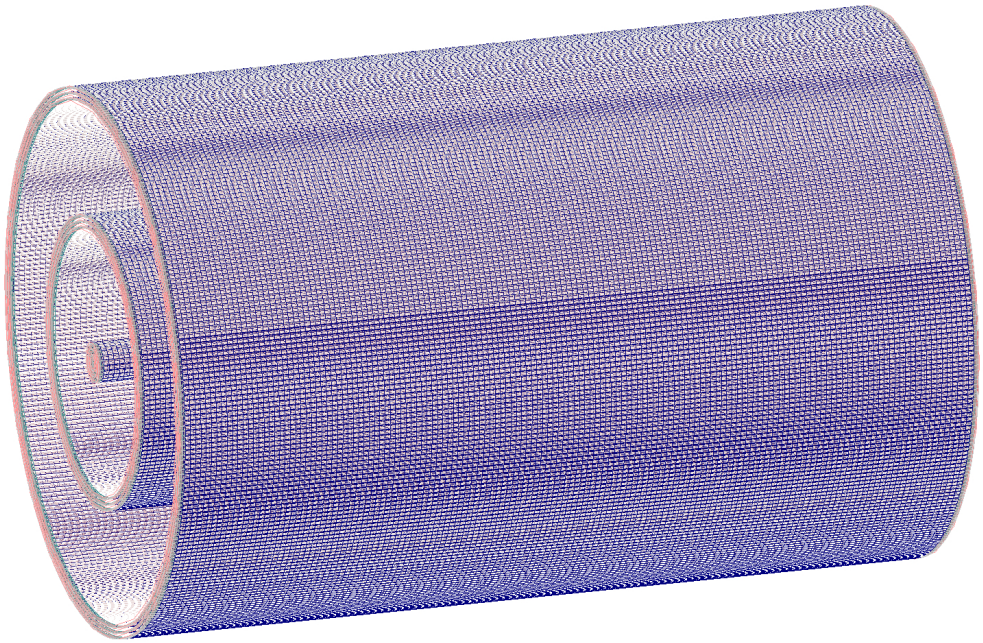

Figure 3.2: The simulated detector with three detector-layer triplets. The picture was generated with the built in simulation display of the Mu3e-framework [13]

.

Beampipe

For the simulation study a 0.8mm thick Beryllium beampipe with an inner radius of 20mm, as proposed for the ATLAS detector upgrade, is used. The beampipe is evacuated. Beryllium provides ideal properties for this usage due to its large radiation length of $X_{0,\mathrm{Be}} = 65.19\mathrm{g/cm}^2$ which makes it penetrable with nearly no interaction for the projectiles. Moreover, the material is well suited for the extreme conditions of ultra high vacuum.

Detector Layers

The realistic layout of detector layer would consist of the sensor itself mounted on a structural element such as a Kapton flexprint in combination with a cooling system. A typical implementation of the cooling structure is in a Kapton- or carbon-foam where CO_2 is circulating and transporting the heat. The foam has besides structural features the task to distribute and conduct the heat equally. An illustration of this realistic setup is shown in figure 3.3.

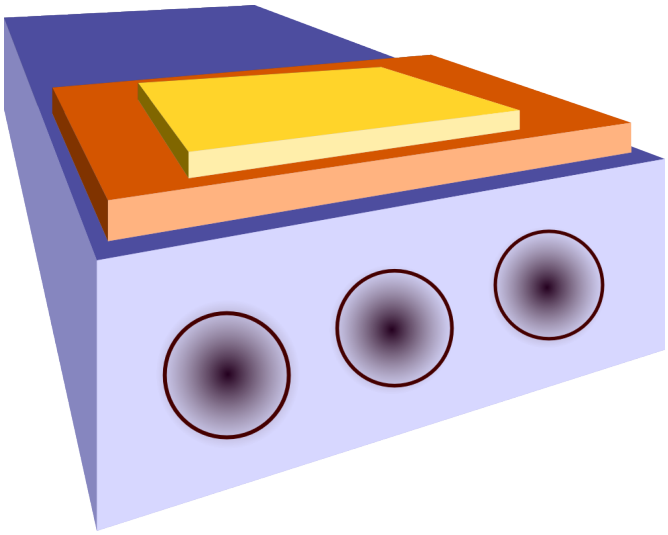

Figure 3.3: Illustration of a realistic layout of a detecor layer showing the sensor on top (yellow), the Kapton structure underneath (red) and the carbonfoam in blue. The circles represent the cooling tubes through which CO_2 is circulating.

The existing Mu3e simulation, has already a defined detector layer set up. Therefore, this provided structure will be used and modified such that it matches the requirements of our cases. In the following the given detector layer composition is depicted.

Each detector layer is made up by a certain number of sensor ladders. A sensor ladder is a strip composed of HV-MAPS silicon sensors (see Chapter 3.1) which are mounted and bonded on a Kapton flex-print and glued to a Kapton frame. So far this

complies with the composition of the Mu3e detector which is in detail described in [13]. In contrast to this setup, however, the conducting aluminum trace is homogeneously distributed on the Kapton in order to increase the accuracy of the calculation of the total single layer radiation length. The modified composition table from ([13] Tab.10.2) is illustrated in Table 3.1.

Table 3.1: The composition of a detector layer is varied by the thickness of the aluminum traces as an artificial placeholder in order to allow different radiation lengths.

Component		Thickness	[μm]		x/X_0	[%]
Kapton frame		25			0.018	
Kapton flex-print		25			0.018	
Aluminum traces	7.5	807.4	1696.7	0.008	0.908	1.908
HV-MAPS		50			0.053	
Adhesive		10			0.003	
Full detecor layer	117.5	917.4	1806.7	0.1	1.0	2.0

It needs to be stressed that this thesis does not aim at studying this exact composition which was maintained rather for the sake of an already well functioning system. This is completely valid, since the only interesting parameter is the total radiation length of the ladder. To study the effects of different material budgets on the track parameter resolution the aluminum thickness is used as an artificial parameter to vary the radiation length. Otherwise, there is no reason for having such a thick conducting trace. It is rather used as dummy material or placeholder in order to reach the radiation lengths that are to be investigated. As one can see there were three aluminum thicknesses and thereby radiation lengths chosen.

1. **Ideal detector.** The relative radiation length of 0.1% represents in most ways an ideal detector, being almost invisible for the particles. This represents the goal of the Mu3e-Experiment [13] which exploits the HV-MAPS technology and helium gas cooling. For this thesis it serves as a zero-level reference.

2. **Next generation detector.** The relative radiation length of 1% is the main object of study. Reaching this goal is possible due to the fast progress in pixel-detector technology and cooling systems over the last years. The radiation length is mainly due to the mechanical support structure and the cooling system as illustrated in Figure 3.3.

3. **Nowadays detector.** A relative radiation length of 2% is a good figure of merit of what is used in todays general-purpose inner detecor systems at LHC. Therefore, this measurement shows a reference point to nowadays standards.

As mentioned, the nine layers of the detector form three groups of detector-layer triplets. The term detector ladder, which is used in this context, pictures the assembly of the sensors with an overhang of 1mm to increase the efficiency by covering the dead zone where the sensors read-out electronics is placed. This overhang can be seen in Figure 3.4 (b), where the sensors are illustrated as thin blue lines. The frame-structure is shown in grey and the evacuated beampipe in green. The red lines represent the so-called mother volume that *Geant4* reserves for the detecor ladder objects.

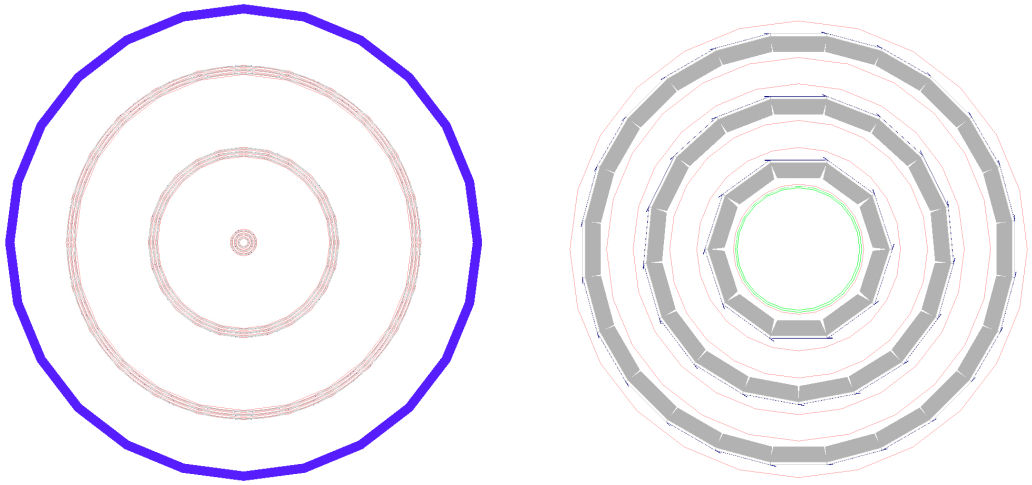

(a) All three detector triplets plus magnet (blue).

(b) Innermost detector triplet plus beampipe (green).

Figure 3.4: Figure (a) illustrates the transverse view on all three detector triplets plus the magnet (blue). Figure (b) shows the transverse view on the innermost detector triplet which can be seen in Figure (a) as the three red circles closest to the centre. One can see the substructure described in 3.2.1. The green circle closest to the centre shows the evacuated beampipe.The pictures were generated with the built-in simulation display of the Mu3e-framework [13].

Each detector layer has a total length of 3m, composed of 150 sensors with a length of 2cm each. The radius at which a layer is positioned depends on its number of sensor ladders which are placed parallel to each other and in direction of the beamline with the described overhang. There is no need to discuss the exact calculation to determine the radius for a certain ladder number here; rather the fact is stressed that one cannot simply choose an integer radius, but has to vary the number of ladders used for a layer. The radii used are summarised in Table 3.1.

Table 3.2: The radii where the sensors of the individual layers are placed in dependency of the number of ladders.

Layer	1	2	3	4	5	6	7	8	9
#Ladder	10	17	24	168	175	182	326	333	340
Radius [mm]	28.6	49.6	70.4	494.7	515.3	535.9	959.9	980.5	1001.2

Magnet

The magnet implemented provides a homogeneous and constant field in z-direction (the coordinate system is clarified in Section 3.3.1, hence, parallel to the beamline. Again, aiming at making an easy comparison with current LHC experiments possible, the magnetic field strength was chosen to be 2.0 Tesla, similar to that of ATLAS.

3.2.2 Particle Generation

The Geant4 toolkit has an implemented event structure which allows the generation of particles by setting their initial position- and momentum-three-vectors. The particle is determined by a string or its PDG-encoding [17]. For this study three different particle types where generated: positive muons, positrons and positive pions due to their representative nature explained in Chapter 2.

Definition of the Coordinate System

The coordinate system is chosen such that the z-direction is parallel to the beamline and that the origin is located at the centre of the detector. Due to the polar symmetry of the detector there would be no need to define the explicit direction of the x- and y-coordinates. However, for reasons of compliance with the exemplary LHC setup, the system is right-handed, with the y-axis pointing upwards. The polar coordinates are denoted by the azimuthal angle ϕ and the polar angle θ to differentiate from the local track parameters. The particle direction at the origin is denoted by Θ_{vtx} and Φ_{vtx}.

Generated Angles and Three-Momenta

For tracking studies single particles are generated from the centre of the detector with initial coordinates $(0, 0, 0)$ with a flat randomised distribution over $\phi_{vtx} \in [0, 2\pi]$ and $\theta_{vtx} \in [7/18\pi, 11/18\pi]$ corresponding to a pseudorapidity of $\eta \in [-0.3564, 0.3564]$ which is illustrated for muons at 1GeV in Figure 3.8. For this study track resolutions are compared for a momentum of $p = 1\text{GeV}/c$.

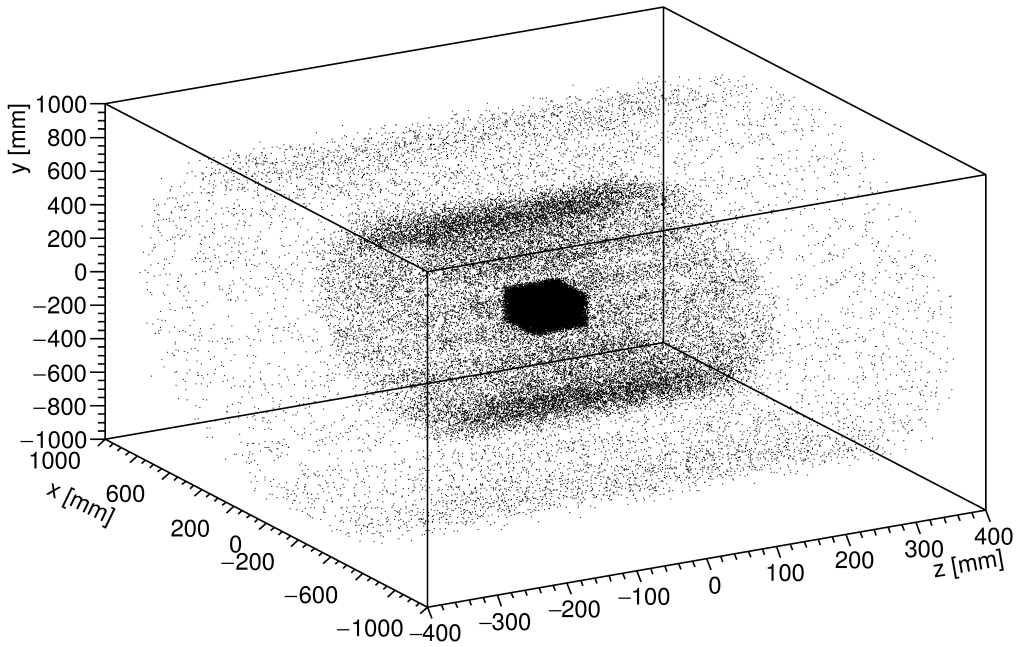

Figure 3.5: 10000 muon hits, generated with 1GeV and $\phi_{vtx} \in [0, 2\pi]$ and $\theta_{vtx} \in [7/18\pi, 11/18\pi]$

.

3.3 Track Reconstruction

As illustrated in the beginning of this chapter, the reconstruction of particle tracks represents the link between collision events and data-analysis. The appropriate algorithm to reconstruct and fit a track has to include track uncertainties due to the finite spatial resolution of a detector and multiple scattering effects due to the interaction with the detector material. Track fits which take both effects into account and which have been found to be accurate are Kalman filters [18] or General Broken Line fits [19]. The implementation of these fits is however beyond the scope of this thesis. Consequentially, two other fits are used in this study, which either account only the effects of multiple scattering (Triplet fit) or only the hit uncertainties (Single Helix fit). Thus, both effects of measurement uncertainties are studied individually. A comparison for these fits with the general solution of the Broken Line Fit has been done by [20] and is shown in figure 3.6 where one can see that the performance for the general broken line fit is overall the best and the single helix fit is better in terms of resolution for higher momenta.

In this section first a hit triplet is described, then the Triplet fit and Single Helix fit are briefly explained as well as the source of possible fake tracks in the reconstruction.

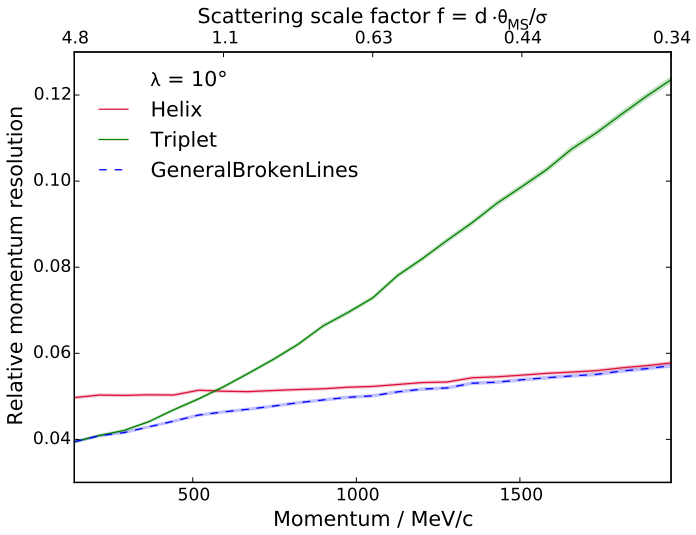

Figure 3.6: Comparison of Single Helix fit (red), Triplet Fit (green) and Broken Line fit (blue). For higher momenta the helix fit is more accurate than the Triplet Fit. The best performance is given by the Broken Line Fit.

Then the algorithm to find and link tracks is discussed and lastly a trigger application made possible by this detector design is portrayed.

3.3.1 Hit Triplet

Hit triplets play a substantial role in this study since the detector design as well as the main track fit used for the particle reconstruction is based on this concept. The special feature of a single hit triplet is that it allows a full determination of a charged particle track in parameter a homogeneous magnetic field.

An undisturbed charged particle follows a helix in an homogeneous magnetic field. This helix is described by seven parameters which are: three spatial coordinates of the starting point, two angles to specify the direction, the curvature (which is in direct relation to the momentum of the particle), and the length of the helix.

Due to the multiple scattering on the middle layer of a detector triplet the particle is deflected from its original path. Therefore, two helix parametrisations are needed to describe the trajectory of the particle. Since the two helices share the point at the scattering layer, eleven parameters remain to be determined. This number is reduced to ten by assuming that the energy loss and hence the change in curvature is negligible or corrected for. A constraint fit is performed, assuming that the average scattering angle vanishes, to determine the track parameters [16]. The constraint fit introduces a bias towards small scattering angles, which is resolved in the next section.

3.3.2 Three-Dimensional Triplet Fit

The triplet fit accounts multiple scattering effect as the primary source of measurement uncertainty and neglects the hit uncertainty which is due to the finite size of the sensors. It is also referred to as multiple scattering fit. Consequently, the fit is tailor-made for modern pixel detectors with high granularity in a large momentum range. As explained in 3.1 the pixel size in this study was chosen to be $80\mu\text{m} \times 80\mu\text{m}$ which makes the hit uncertainty not fully negligible for high momentum tracks. In this region a second fit is described in the next section 3.3.3.

For the triplet fit a triplet of three hits with precise knowledge of the coordinates is constructed, see Figure 3.7. The three points are connected by two helices. The three-dimensional triplet fit aims to describe a particle trajectory in a solenoidal homogeneous magnetic field considering multiple scattering at the detector layers and is in full detail described in [21]. The scattering effects are as well taken into account by Kalman Filters [18] and General Broken Line fits [19]. In contrast to these two approaches this fit is non-iterative and highly parallel. This makes it very fast and well suited for online track reconstruction and trigger applications. The speed of the fit will not be investigated here, neither compared with the other two. The reason for its usage is the fast computation time and the suitability to this detector design which is, too, consisting of triplets in the sense of closely stacked detector layers.

The parameters used in the fit are illustrated and depicted in 3.7. An underlying assumption of this method is that the material responsible for the multiple scattering deflection lies in the same plane where the hit is measured which is valid for modern silicon sensors.

Obviously, the triplet fit needs at least three hits to function. In case that more than three hits are fitted a series of triplets is formed as illustrated in Figure 3.8. This reduces the bias towards small scattering angles which was introduced with the necessary assumption that the average scattering angle vanishes. The number of triplets is given by $n_{hits} - 2$, where n_{hits} is the number of hits in a track.

Some of the main characteristics of the fit [21] are mathematically portrayed in the following. The goal of the fit is to determine the three-dimensional radius R_{3D} of the global helix that minimises the value of χ^2 which is given by

$$\chi^2(R_{3D}) = \frac{\Theta^2_{MS}(R_{3D})}{\sigma^2_\Theta} + \frac{\Phi^2_{MS}(R_{3D})}{\sigma_P hi^2}, \tag{3.1}$$

with the constant variances σ^2_Θ and σ^2_Φ. One of the main features of the fit algorithm is that with the assumption that the standard variations are equal - ergo denoted as

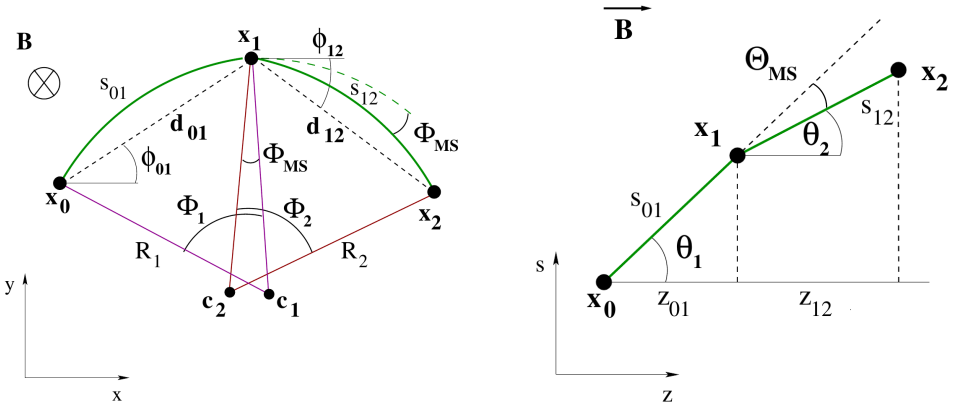

(a) Triplet fit Parameters, illustrated in the transverse plane.

(b) Triplet fit Parameters, illustrated in the longitudinal plane.

Figure 3.7: Definition of parameters used in the triplet fit which takes the multiple scattering at the middle layer into account, here at point $\vec{x_1}$. The hits at first and third layer are $\vec{x_0}$ and $\vec{x_2}$, respectively. The arc length between $\vec{x_0}$ and $\vec{x_1}$ is s_{01} and between $\vec{x_1}$ and $\vec{x_2}$ it is s_{12}. The transverse track and hence circle radii are R_1 before and R_2 after scattering with the bending angles Φ_1 and Φ_2. The transverse multiple scattering angle is denoted as Φ_{MS}. The connection between the first and second two points is given by $\vec{d_{01}}$ and $\vec{d_{12}}$, respectively, with their corresponding azimuth angles ϕ_{01} and $\phi 12$. The longitudinal arc polar angles are given by θ_{01} and θ_{12}, the distances between the first two and second two hits in z-direction by z_{01} and z_{12} and the multiple scattering angle in the longitudinal plane by Θ_{MS}. Taken from [21].

a single variable $\sigma_{MS} = \sigma_{Theta} = \sigma_{Phi}$ in the following - the minimisation criterion simplifies to

$$0 \stackrel{!}{=} \frac{\mathrm{d}\Theta_{MS}}{\mathrm{d}R_{3D}}\Theta_{MS} + \frac{\mathrm{d}\Phi_{MS}}{\mathrm{d}R_{3D}}\Phi_{MS}, \tag{3.2}$$

which allows to calculate the multiple scattering uncertainty *after* the triplet is fitted. The average 3D-radius of a track composed of a series of triplets is then given by:

$$\overline{R_{3D}} = \sum_{i}^{n_{hit}-2} \frac{R_{3D,i}}{\sigma_i(R_{3D})^2} \Big/ \sum_{i}^{n_{hit}-2} \frac{1}{\sigma_i(R_{3D})^2}, \tag{3.3}$$

where $\sigma_i(R_{3D})$ is the uncertainty of the corresponding 3D-radius:

$$\sigma(R_{3D}) = \sigma_{MS} \sqrt{\frac{1}{(\frac{\mathrm{d}\Phi_{MS}}{\mathrm{d}R_{3D}})^2 + (\frac{\mathrm{d}\Theta_{MS}}{\mathrm{d}R_{3D}})^2}}. \tag{3.4}$$

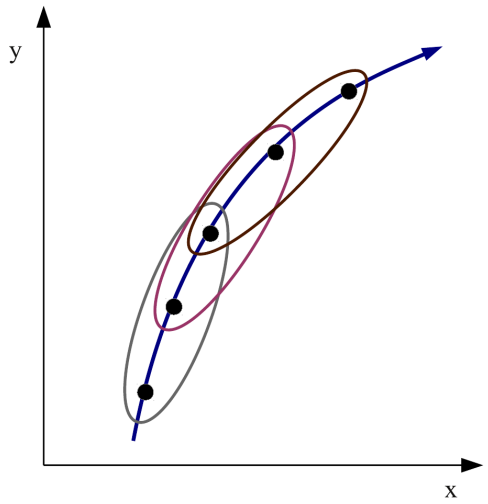

Figure 3.8: In case of more than three hits the triplets used for the fit are composed of overlapping triplets. Taken from [21].

.

Thus, the uncertainty of the fitted radius is given by:

$$\sigma(\overline{R_{3D}}) = \left(\sum_{i}^{n_{hit}-2} \frac{1}{\sigma_i (R_{3D})^2} \right)^{-1/2}. \tag{3.5}$$

Furthermore, the uncertainties of the polar and azimuthal angle are:

$$\sigma(\Phi_i) = \sigma(\overline{R_{3D}}) \left| \frac{\Phi_i}{R_{3D,i}\alpha_i} \right|, \tag{3.6}$$

$$\sigma(\Theta_i) = \sigma(\overline{R_{3D}}) \left| \frac{\cot\Theta_i}{R_{3D,i}(1-\alpha_i)} \right|, \tag{3.7}$$

which will be relevant in the track linking in Section 3.3.4. Here, α_i denotes the index parameter which links the polar and azimuthal angles to the 3D-radius:

$$\left. \frac{\mathrm{d}\Phi_i}{\mathrm{d}R_{3D}} \right|_{R_{3D}} = -\alpha_i \frac{\Phi_i}{R_{3D}}, \tag{3.8}$$

$$\left. \frac{\mathrm{d}\Theta_i}{\mathrm{d}R_{3D}} \right|_{R_{3D}} = (1-\alpha_i) \frac{\cot\Theta_i}{R_{3D}}. \tag{3.9}$$

3.3.3 Single Helix Fit

In this thesis tracks up to an energy of 100GeV are studied where the assumption that material effects dominate over hit uncertainties does not hold true any longer. Hence,

for high-energy tracks the Karimäki fit [22] is used, that only regards hit uncertainties due to the finite pixel resolution.

The fit used for this task assumes a single helix for the entire particle trajectory. Therefore, the fitting can be done separately in the transverse (x, y)-plane, where the helix is projected as a circle, and a straight line in the longitudinal plane, defined by the track length s and z. For the straight line fit the least-square method is used. The circle fit is implemented using Karimäki's method [22]. Here, the least-squares problem is formulated:

$$\chi^2_K = \sum_i w_i \epsilon_i^2, \tag{3.10}$$

where w_i are weights and ϵ_i the residuals orthogonal to the track:

$$\epsilon_i = \pm\Big[\sqrt{(x_i - a)^2 + (y_i - b)^2} - R\Big]. \tag{3.11}$$

where x and y are the two-dimensional coordinates of the hit and a and b those of the circle centre with radius R. Karimäki's ansatz is to assume that $|\epsilon_i| \ll R$ which simplifies Equation 3.7 to:

$$\epsilon_i \approx \pm\frac{1}{2} R^{-1}\Big[(x_i - a)^2 + (y_i - b)^2 - R^2\Big], \tag{3.12}$$

thereby linearising the minimising problem.

3.3.4 Track Linking

The linking of hits to a full track requires an adequate and fast algorithm to tackle the combinatorial problem. Triplet fits are used for track linking as they work for low and high transverse momenta for the studied design. Additionally, the triplet fit can be modified to include hit uncertainties. However, this was not used for this study.

Track Seed and Triplet Sets

First of all, a track seed is needed when linking to a full track. The track seed is in our case the hit triplet of the innermost three detector layers since those already define all track parameters. Linking of the hits in a triple-layer is rather simple since the tracks are nearly straight and the distances between the layers are only 2cm. Therefore, only a small search window can be used which makes the method very fast. When three hits are linked, the triplet fit is applied to calculate the track parameters.

The linking of hit triplets is analogously done for the second detector triple layer and the third detector triple layer. As a result, for a full set of nine hits only three hit

triplets have to be linked. Starting from the innermost triplet, the track seed, to the second triple layer and to the third. The algorithm is illustrated in the following.

Triplet Linking for the Multiple Scattering Fit

The main task of the algorithm is the linking of the three triplets to complete tracks. Here, a correct assignment of triplets is crucial since wrong combinations impairs the purity of the set of reconstructed tracks [2]. However, what makes this detector design stand out is the mentioned full set of track parameters available already with the track seed. By linking the inner triplet to the outer triplets the precision of the track parameters is highly increased.

In order to lengthen the lever arm of the track seed and to improve the linking a beamline constraint is applied. This is done by extrapolating from the innermost layer to the distance of closest approach (dca) and setting x- and y-coordinate to zero while leaving the z-coordinate (z_0) untouched such that a fourth hit is added with the coordinates $(0, 0, z_0)$. This is valid if we now that the particle originates from the beamline. If that is not the case in a scenario considering secondary particles, this beamline constrained cannot be applied.

Using this long lever arm the helix is extrapolated from the first hit triplet including the beamline constraint to the second hit triplet at layers 4, 5 and 6. The starting point of the helix is the third detector layer. The intersection point at the fourth layer defines the centre on the next detector layer around which a window is defined. If there is a hit located in this window, a track of six hits is formed consisting of the first triplet without the constraint point and the second triplet. This hit series is fitted to see if the two triplets belong to a single track or are falsely connected.

The determination of the optional search window size in which the first hit of the next triplet is searched for is not trivial. It is optional in the case only a single particle is reconstructed but since the reconstruction algorithm is not only aiming for that special case it is taken into account. Due to the non-linear correlation of the track parameters, namely the directional angles Φ and Θ at the last layer and the 3D-radius, the following extrapolation method is chosen. First, the parameter uncertainty is calculated which takes the multiple scattering uncertainty into account as well as the parameter uncertainty from Equations 3.5, 3.6, 3.7. The uncertainty of the 3D-radius is provided by the fit, as well as the uncertainty for Φ and Θ at the middle layer of a detector triplet. For the angles, the total uncertainty is then calculated by

$$\sigma_{-xi,\text{total}} = \sqrt{\sigma_{MS}^2 + \sigma_{\xi,fit}}, \tag{3.13}$$

[2] Purity denotes the relative number of true reconstructed tracks to the number of generated tracks.

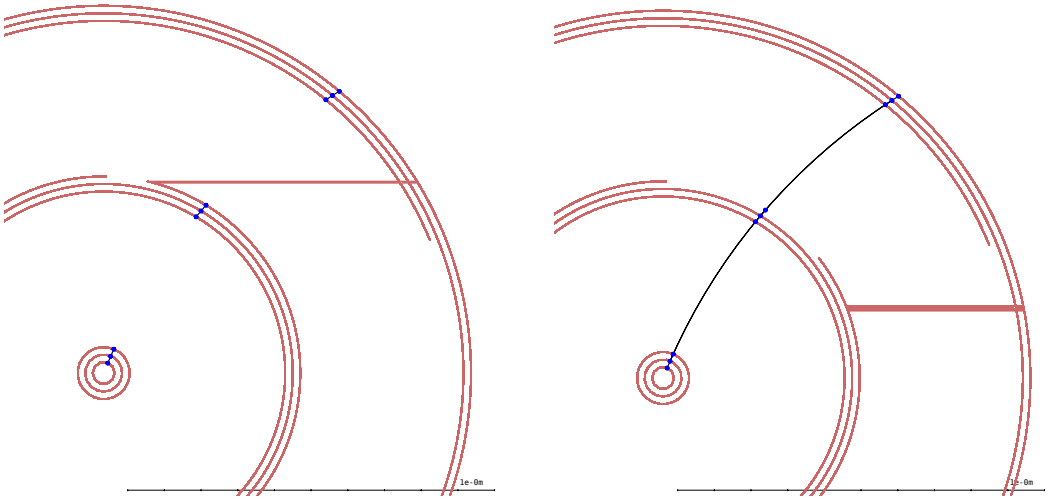

(a) Triplets found for single muon with 1GeV. **(b)** Linked track of a single muon with 1GeV.

Figure 3.9: Hit triplets before and after triplet linking. Generated with the Mu3e-framework event display.

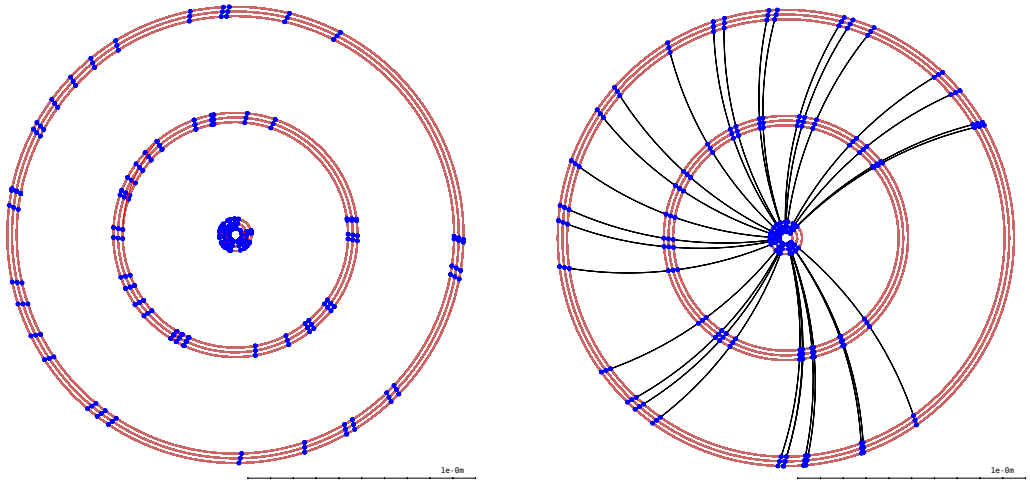

(a) Triplets found for 30 muons with 1GeV. **(b)** Linked tracks of 30 muons with 1GeV.

Figure 3.10: Hit triplets before and after triplet linking for 30 generated muons. Generated with the Mu3e-framework event display.

where ξ is a placeholder for Φ and Θ. Since the extrapolation is non-linear the total uncertainty of the parameters has to be in one case added, in the next case left unchanged, and in the last step subtracted from its corresponding parameter as depicted in Table 3.3. This is done for each of the three parameters R_{3D}, Φ and Θ, which makes a total of 27 different extrapolation variations.

Table 3.3: Extrapolation variation combinations. The three parameters are varied by their uncertainty times a constant c. This variation is added, not added or subtracted, hence, providing 27 different extrapolation possibilities.

	R^*_{3D}	Φ^*	Θ^*
$+$	$R_{3D} + \sigma(R_{3D})$	$\Phi + \sigma(\Phi)$	$\Theta + \sigma(\Theta)$
0	R_{3D}	Φ	Θ
$-$	$R_{3D} - \sigma(R_{3D})$	$\Phi - \sigma(\Phi)$	$\Theta - \sigma(\Theta)$

Further, the length of the window is determined by the minimum and maximum z-coordinate, thus, defining the allowed longitudinal range. The angular difference of in the transverse plane is given by the difference in $\Delta\Phi$ which is defined as:

$$\Delta\phi = \text{atan}(\frac{y_{\text{unvaried}}}{x_{\text{unvaried}}}) - \text{atan}(\frac{y_{\text{varied}}}{x_{\text{varied}}}), \tag{3.14}$$

This window is furthermore linearly widened by simply multiplying the maximum and minimum boarders corresponding to the 1σ size envelop of the window with a constant c_{cut}.

In Figure 3.11 the number of reconstructed tracks is shown in dependence of the c_{cut} factor. The red line marks the 100% since in total 10^5 muons were simulated. As one can see the value $c_{cut} = 12$ allows nearly 100% efficiency and has proven to be a good figure of merit in the definition of the extrapolation window. This is especially interesting for the simulation of LHC events were a too wide envelop highly increases the fake rate.

The procedure of extrapolating and adding triplets to the track whose first point is located inside the allowed window is repeated for the last detector triplet and the resulting track consisting of nine hits is fitted.

3.3.5 Fake Hits

Regarding the track reconstruction it is crucial to account for cases with more then one hit per layer produced by a single particle. This may results in two reconstructed tracks for a single generated particle, since a hit is not locked after being linked to a track. In the following two possible ways for the creation of a "doublehit" are illustrated.

Overlap Doublehits

As mentioned in Chapter 3.2.1 the sensors are positioned with an overhang of 1mm relative to each other in order to increase the acceptance of the detector. This repres-

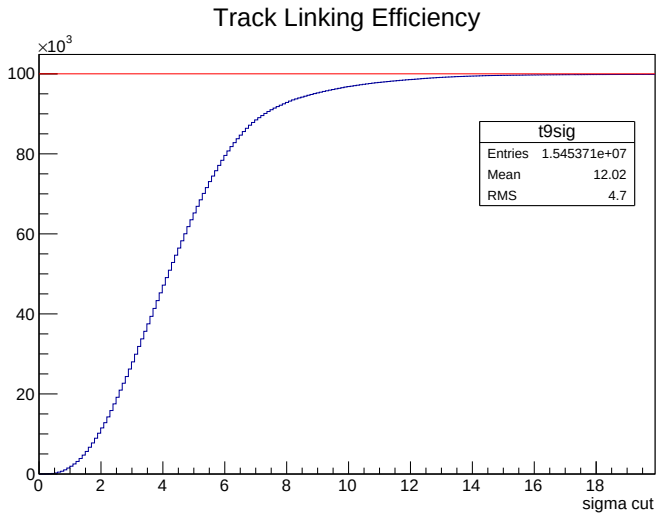

Figure 3.11: Number of reconstructed single muons in dependence of the constant c_{cut} which defines the final size of the extrapolation window. The red line marks the total number of generated muons and hence 100%

ents the major cause for a particle to be detected twice in the same detector layer as illustrated in Figure 3.12.

Pixel Cluster

A pixel cluster denotes an event were a particle traverses adjacent pixels. Due to small thickness of the sensors of 50μm and the straightness of the particle trajectories this can be considered to be an unlikely event.

Resolving Track Ambiguities

The algorithm addresses the multiple reconstruction of a track with a function that merges two tracks into a single one without loosing hits in case of a track ambiguity. That way no information is lost and the same track is not reconstructed twice.

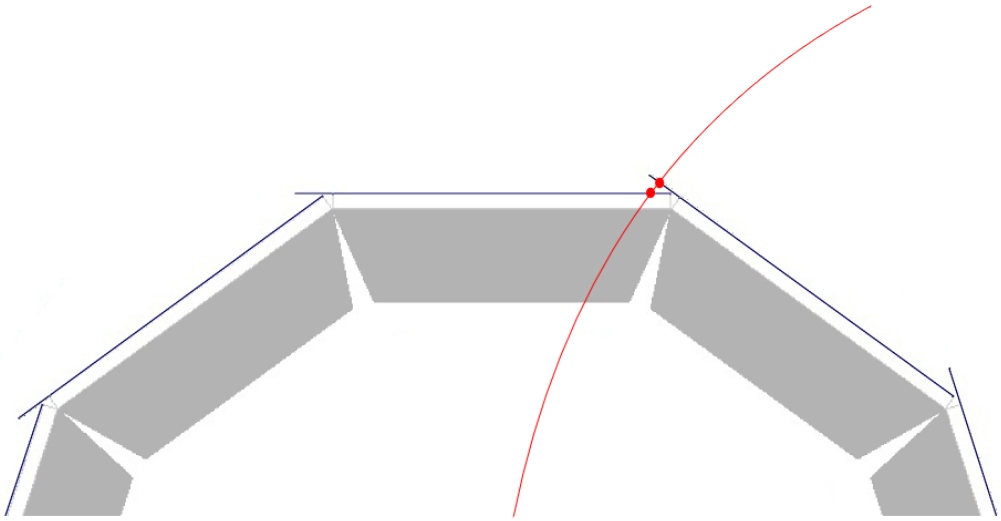

Figure 3.12: Illustration of a particle trajectory (red) causing two hits in the same detector layer. The picture was generated with the built in simulation display of the Mu3e-framework [13] and modified by adding the example trajectory.

4 *triplet3* Trigger

The *triplet3* Trigger offers the ability for fast online track reconstruction and trigger decisions taking advantage of the closely stacked triple detector layers. For this application no change in geometry of the discussed *triplet9* design is needed. The trigger only needs the three outermost detector layers for full functionality.

The advantage of taking the outermost detector triplet lies in the much lower particle rate at this distance of approximately 1m. That is a result of the 2 Tesla strong magnetic field which prevents particles with very low momenta from reaching the trigger. Therefore, an implicit filter is given by the large radius of the trigger layers.

The second reason for using the outermost detector triplet is the large bending arm for reconstructed tracks. As already explained, a triplet of hits is sufficient to determine the track parameters. Therefore, the z-position of the closest approach to the beamline can be determined and used as an extra hit with the coordinates $(0, 0, z_0)$. This approximation can be done because the collision points of the particles deviate very little from the beamline in the transverse direction but can occur on the beamline in a region of several centimetres.

4.1 Trigger Concept

The main challenge for a trigger is the very short time in which a trigger decision has to be made. This trigger decision uses a straight line approximation which is valid for the great majority of tracks in a high-energy collision for closely stacked detector layers. The straight line connects the hit from the first and third layer. By spanning again a window around the intersection point of the straight line with the middle layer, one can define a criterion for the acceptance or rejection of a track candidate depending on the positioning of the middle hit in- or outside this window [1].

4.1.1 p_T-Cut

Once a triplet is found the fast track reconstruction mentioned above is applied to obtain the parameters.When the triplet and hence the track parameters are known, the slope of the track can be determined which is defined as:

[1] *Personal communication*, A. Schöning, Feb. 2015

$$\phi'(r) = \frac{\phi_9 - \phi_7}{2\Delta r} = \frac{\Phi}{2}, \tag{4.1}$$

where ϕ_9 and ϕ_7 denote the ϕ of the seventh and ninth layer as defined in (**??**), Δr is the distance between the layers and Φ the angle that determines the transverse position of the particle. Due to the relation given in (4.1) one can now directly determine the transverse track radius r_T using

$$\frac{r_8}{2\phi'} = \frac{r_8}{\Phi} = r_T, \tag{4.2}$$

where r_8 is the radius of the eighth layer. Thereby the transverse momentum resolution is obtained due to $r_T \propto p_T$. As a result, one can easily apply a $p_{T,min}$ cut when setting a maximum value for the slope ϕ'_{max}.

4.1.2 Vertex-Cut

The other advantage of the *triplet3* trigger is the direct reconstruction of the z-position at the vertex z_{vtx} by using the relation

$$z'(r) = \frac{z_9 - z_7}{2\Delta r}, \tag{4.3}$$

where the indices again denote the layer number of the parameter. That makes the direct calculation of z_{vtx} possible by using:

$$z_{vtx} = z_7 - r_7 \cdot z'. \tag{4.4}$$

With the knowledge of z_{vtx} two more trigger decisions can be applied. Firstly, a cut for secondary particles when requiring $|z_{vtx}| < z_{vtx}^{\text{cut}}$ for a previously defined cut value. For range of 20mm where collisions can occur on the beam axis a cut of 1mm would already reduce the bunch region by a large factor.

And secondly, a two-lepton trigger possibility exists when using $|z_{vtx,1} - z_{vtx,2}| < z_{\text{cut}}$ where the pileup can be highly reduced by determining whether two particles were originating from the same vertex.

5 Reconstruction Results and Discussion

This chapter presents the results obtained in this thesis. In particular the track parameter resolution for positive muons, positrons and positive pions is portrayed with regard to the individual characteristics of the particles. The results are presented for two different fit models.The momentum-, Θ_{vtx}- and Φ_{vtx}- resolution is studied for momenta up to 100 GeV. For high momenta the single helix fit is used as multiple scattering effects are negligible.

As previously mentioned in Chapter 2 the three particles μ^+, e^+, π^+ were chosen in order to represent the different particle interactions. The muon (in this context muon refers to μ^+) is a particle that due to its mass of 105.7MeV/c^2 penetrates matter with little interaction. Muons do not participate in electromagnetic and strong interactions which allows to treat them as minimum ionising particles. For these reasons, the muon marks in many ways the benchmark particle when it comes to track reconstruction.

The positron's interactions greatly differ from those of the muon. The major cause of energy loss in our investigated energy range is due to Bremsstrahlung.

The third particle that is investigated is the positive pion. This particle was chosen because it is the most frequently produced in hadron colliders and is often produced as a secondary particle. In addition, it represents the class of the hadrons which undergo hadronic interactions with the detector material.

5.1 Track Parameter Resolution at 1GeV

In order to determine the capabilities of the *triplet9* detector design which consists of three groups of closely stacked triple detector layers, the reconstructed track parameters are compared to the corresponding generated ones. For that purpose, three types of particles, μ^+, e^+, π^+, were generated with a single particle generator. In the following track parameter resolutions are discussed for a typical momentum of $p = 1\text{GeV}/c$. The peculiar value of 1GeV/c was chosen since this momentum corresponds to the majority of particles from pp-collisions at the LHC [16].

In the following, histograms are shown for the resolution of various track parameters. The resolution is defined as the standard deviation of the distribution of

$$\Delta\xi = \xi_{reconstructed} - \xi_{generated}, \tag{5.1}$$

and in the case of the relative parameter resolution of

$$\Delta\xi_{rel} = \frac{\xi_{reconstructed} - \xi_{generated}}{\xi_{generated}}, \tag{5.2}$$

where ξ is placeholder for a track parameter. The y-axis is scaled by $1/n_{entries}$ in order to allow drawing multiple distributions into a single histogram. That said, the resolutions of a particle for the three different material thicknesses $0.1\%X/X_0$, $1\%X/X_0$ and $2\%X/X_0$ are combined in the histogram such that the "zero reference" of $0.1\%X/X_0$ is drawn in blue, the aimed realistic value of $1\%X/X_0$ in green and the comparison value for nowadays detectors of $2\%X/X_0$ in red.

In particular the following parameter resolutions are presented and discussed: the relative transverse radius $p_{T,rel}$, the z-distance of closest approach to the beamline (z_0), the distance of closest approach to the beamline (dca), the polar angle at the origin of the particle θ_{vtx}, and the azimuthal angle at the origin ϕ_{vtx}. To allow a direct comparison of the fits the of the two better resolution is in bold print (or both if the difference between the resolutions is negligible).

5.1.1 Relative Transverse Momentum Resolution

First the resolution of the reconstructed relative transverse momentum $\Delta p_{T,rel}$ is presented.

Figure 5.1 shows the results for the momentum reconstruction of μ^+, e^+ and π^+ in this order from top to bottom. The resolutions on the left hand side were obtained using the multiple scattering fit (see Section 3.3.2), those on the right hand side using the single helix fit (see Section 3.3.3). The root-mean-square (RMS) value which determines the resolution by the width of the distribution is summarised for $\Delta p_{T,rel}$ in Table 5.1.

One can see that the mean values are all shifted to the left and that an increase in radiation length correlates with a wider distribution, hence, a worse resolution. Furthermore, the single helix fit produces better resolutios for the relative radiation length of $0.1\%X/X_0$. For $1\%X/X_0$ and $2\%X/X_0$ the performance of the fits is similar.

5.1.2 Parameter Resolution at Vertex

The track parameters at the origin of the particles determine its initial position and direction.

Since at collision experiments the exact z-position is not known, the parameter of interest is the z-position at the point of closest approach of the reconstructed trajectory

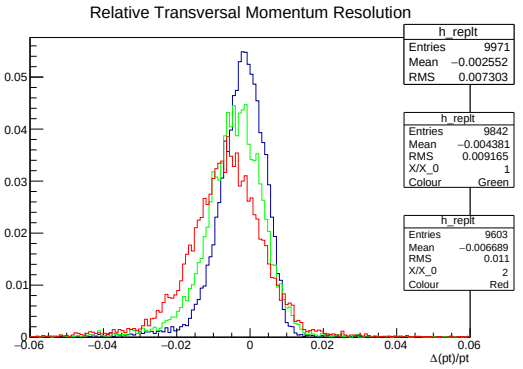

(a) $\Delta p_{T,rel}$ of $p = 1\text{GeV}/c$ muon reconstructed with a multiple scattering fit.

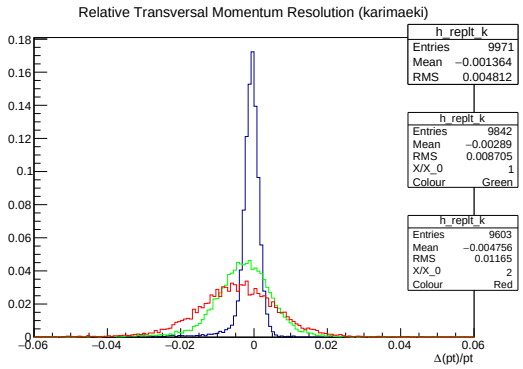

(b) $\Delta p_{T,rel}$ of $p = 1\text{GeV}/c$ muon reconstructed with a single helix fit.

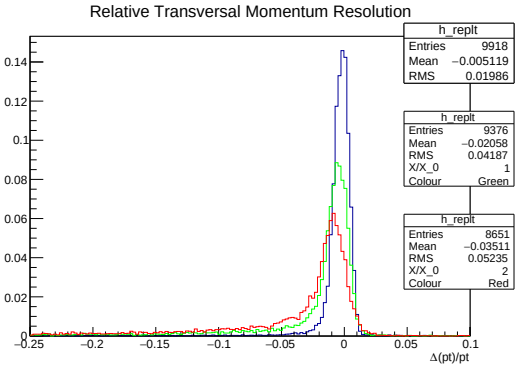

(c) $\Delta p_{T,rel}$ of $p = 1\text{GeV}/c$ electron reconstructed with a multiple scattering fit.

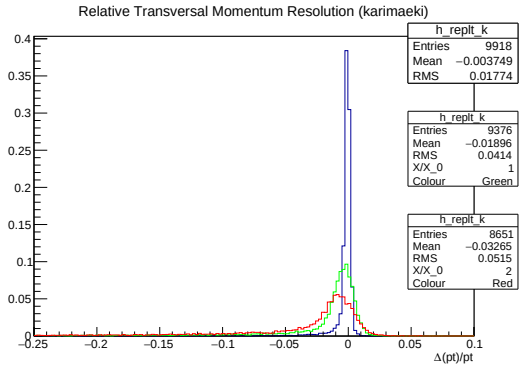

(d) $\Delta p_{T,rel}$ of $p = 1\text{GeV}/c$ electron reconstructed with a single helix fit.

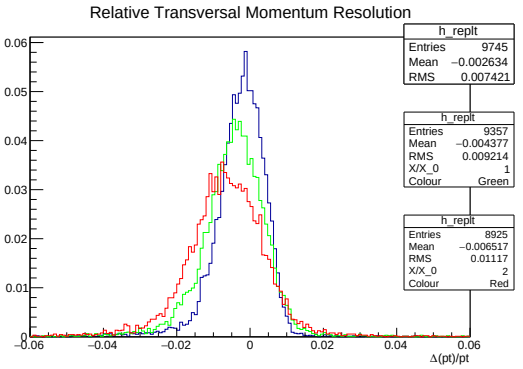

(e) $\Delta p_{T,rel}$ of $p = 1\text{GeV}/c$ pion reconstructed with a multiple scattering fit.

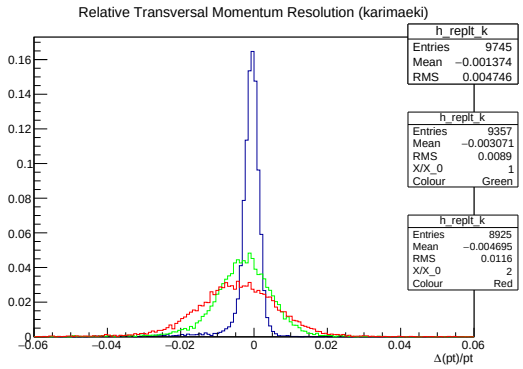

(f) $\Delta p_{T,rel}$ of $p = 1\text{GeV}/c$ pion reconstructed with a single helix fit.

Figure 5.1: Figures (a), (c), (e) show the momentum resolution for generated muons, electrons and pions, respectively, which were obtained by the multiple scattering fit. Similarly for Figures (b), (d), (e), where the single helix fit is used. The distribution for a relative radiation length of $0.1\%X/X_0$ is illustrated in blue, for $1\%X/X_0$ in green and for $2\%X/X_0$ in red.

Table 5.1: Summary of the $\Delta p_{T,rel}$ values illustrated in Figure 5.1.

RMS($\Delta p_{T,rel}$)	MS-Fit			Helix-Fit		
particle	$0.1\%X/X_0$	$1\%X/X_0$	$2\%X/X_0$	$0.1\%X/X_0$	$1\%X/X_0$	$2\%X/X_0$
μ^+	0.0073	0.0092	**0.0110**	**0.0048**	**0.0087**	0.0112
e^+	0.0199	0.0419	0.0524	**0.0177**	**0.0414**	**0.0515**
π^+	0.0074	0.0092	**0.0112**	**0.0047**	**0.0089**	0.0116

to the beamline. At LHC the x- and y-coordinates of the collision point are not precisely zero due to the finite transverse cross section of the particle bunches. However, they are so small that their value is negligible. Therefore, by good approximation the origin of the particle in a LHC-like experiment is $(0, 0, z_0)$. Consequently, one can determine if a track belongs to a primary or secondary vertex if z_0 is reconstructed. Additionally, in case of events with large pileup (number of collisions in an event) the z_0 specifies to which of the individual collisions a particle belongs to. The distributions of the reconstructed z_0-position are shown in Figure 5.2 and the resolutions are summarised in Table 5.2.

Table 5.2: Summary of the Δz_0 values illustrated in Figure 5.2.

RMS(Δz_0)	MS-Fit			Helix-Fit		
particle	$0.1\%X/X_0$	$1\%X/X_0$	$2\%X/X_0$	$0.1\%X/X_0$	$1\%X/X_0$	$2\%X/X_0$
μ^+	**0.0676**	**0.0779**	**0.0901**	0.0805	0.2644	0.3733
e^+	**0.0668**	**0.0799**	**0.0916**	0.078	0.254	0.339
π^+	**0.0698**	**0.0852**	**0.0973**	0.0801	0.2648	0.3673

Figure 5.2 shows the resolution of the reconstructed z_0 position and Figure 5.3 shows the resolutions for the *dca*. For both the resolutions are symmetrically distributed around zero. The dependency of the radiation length on the multiple scattering fit is small, especially regarding the single helix fit whose performance drastically decreases at high radiation lengths. Overall, the multiple scattering fit provides better results with a resolution of about $\sigma(z_0) \sim 80\mu$m and $\sigma(dca) \sim 95\mu$m.

Table 5.3: Summary of the *dca* values illustrated in Figure 5.3.

RMS(*dca*)	MS-Fit			Helix-Fit		
particle	$0.1\%X/X_0$	$1\%X/X_0$	$2\%X/X_0$	$0.1\%X/X_0$	$1\%X/X_0$	$2\%X/X_0$
μ^+	**0.0707**	**0.0872**	**0.1005**	0.0713	0.1259	0.1692
e^+	**0.0743**	**0.1027**	**0.1292**	0.0785	0.1846	0.2431
π^+	**0.0718**	**0.0876**	**0.1063**	0.0715	0.1249	0.1741

Table 5.4: Summary of the $\Delta\Phi_{vtx}$ values illustrated in Figure 5.2.

RMS($\Delta\Phi_{vtx}$)		MS-Fit			Helix-Fit	
particles	$0.1\%X/X_0$	$1\%X/X_0$	$2\%X/X_0$	$0.1\%X/X_0$	$1\%X/X_0$	$2\%X/X_0$
μ^+	0.0022	**0.0028**	**0.0032**	**0.0015**	**0.0029**	0.0038
e^+	0.0024	**0.0038**	**0.0048**	**0.0019**	0.0046	0.0060
π^+	0.0022	**0.0028**	**0.0033**	**0.0014**	**0.0027**	0.0036

Table 5.5: Summary of the $\Delta\Theta_{vtx}$ values illustrated in Figure 5.2.

RMS($\Delta\Theta_{vtx}$)		MS-Fit			Helix-Fit	
particles	$0.1\%X/X_0$	$1\%X/X_0$	$2\%X/X_0$	$0.1\%X/X_0$	$1\%X/X_0$	$2\%X/X_0$
μ^+	0.00167	**0.00207**	**0.00245**	**0.00094**	0.00254	0.00352
e^+	0.00170	**0.00211**	**0.00252**	**0.00101**	0.00266	0.00377
π^+	0.00167	**0.00208**	**0.00249**	**0.00095**	0.00258	0.00355

The resolutions of the azimuthal and polar angles, Φ_{vtx} and Θ_{vtx} are shown in Figure 5.4 and 5.5 and resolutions are summarised in Tables 5.4 and 5.5. For Φ_{vtx} a minimal shift of the mean values to more negative values can be seen, however, only in the multiple scattering fit results. Θ_{vtx} is characterised by a very thorough gaussian shape whereas Φ_{vtx} features minor asymmetries in from of a small tail to the left. Again, the multiple scattering fit is more stable and provides better resolutions regarding the two higher radiation lengths. The single helix fit resolutions are only better for the reference radiation length of $0.1\%X/X_0$.

5.1.3 Discussion of the Parameter Resolution at 1GeV

Particle Comparison

First of all, the differences of the individual particle types are apparent, especially for e^+. In terms of shape and resolution the reconstruction of the muon and pion are nearly equivalent with only fourth digit discrepancies in favour of the muon. This stresses the statement of Chapter 2 that hadronic interactions only play a minor role in this set-up. From this fact one can already draw a conclusion, namely, that the reconstruction of highly realistic hadrons performs equally well as the reconstruction of the μ^+.

Moreover, one can see the gaussian shape for the $\Delta p_{T,rel}$-distribution of the μ^+ and π^+. In first order the shape of the distribution for the e^+ is similar to the other two particles. This accounts the multiple scattering that occurs as well for the electron. A major difference of the electron distributions is their long tail to the left for the reconstructed transverse momentum. Bearing Equation (5.1) and (5.2) in mind, a

negative value in the histogram correspond to a reconstructed value that is lower than the generated one. Therefore, the tail perfectly demonstrates the dominant energy loss of the electrons due to Bremsstrahlung at momenta of 1 GeV.

Another characteristic feature is the shift of the peak position of the Δp_T distribution to the left. as explained above, this correlates to the energy loss which is proportional to the material thickness. In addition, the increase in the thickness of the material broadens the distribution and thereby worsens the resolution. This is a direct result of the higher chance of a particle to be scattered to wider angles for larger material thickness.

The resolution distribution of the vertex parameters z_0, dca, Φ_{vtx}, and Θ_{vtx} are discussed in the following and are shown in Figures 5.2, 5.3, 5.4 and 5.5 respectively. Apart from $\Delta\Phi_{vtx}$ no shift to the left in the track vertex parameters is visible. This demonstrates that energy loss is not relevant for the vertex parameters z_0, dca and Θ_{vtx}. The vertex parameter Φ_{vtx} is on the other hand related to energy loss since it increases the curvature of the track. As a result, the overall radius is reconstructed systematically too large which leads to a systematically smaller reconstructed value for Φ_{vtx} which can be nicely seen in Figures 5.4 (a),(c),(e).

Fit Comparison

The effect of multiple scattering on the fit results are much more dramatic for the single helix fit then for the multiple scattering fit. For the lowest relative radiation length of $0.1\%X/X_0$ the performance on the reconstruction of the transverse momentum is much better when applying the single helix fit which only takes hit uncertainties into account. However, for detector layers with a relative radiation length of 1 and 2 $\%X/X_0$, the momentum resolution of both fits its comparable [1].
In the case of the vertex parameters the performances of the fits are different. The reconstruction of z_0 and dca is much more precise when using the multiple scattering fit. For Φ_{vtx} and Θ_{vtx} at $0.1\%X/X_0$ the single helix resolution results are better, whereas for 1% and 2% radiation length the performance of the multiple scattering effect is superior. The reason that the single helix fit provides better resolutions for $0.1\%X/X_0$ is due to the fact that it takes account for hit correlations whereas the multiple scattering fit looses them when regarding only one hit triplet at a time.

This conclusion, of course, is only valid for the momentum of 1GeV. With lower momenta the multiple scattering measurement uncertainty becomes dominant towards

[1] The single helix fit directly reconstructs the transverse momentum. On the contrary, the multiple scattering fit determines the momentum, hence the transverse momentum is given by $p_{T,\text{MS-Fit}} = p_{\text{MS-Fit}} \cdot \cos\theta_{vtx}$ which includes the error of the reconstructed θ_{vtx}, the polar track angle.

the hit uncertainty. Even more relevant is the argument of the pixel-size. As explained in Chapter 3 the pixel size used in this study is $80\mu\text{m} \times 80\mu\text{m}$. The estimated size of a modern pixel detector can reach $40\mu\text{m} \times 40\mu\text{m}$ or even less. In this case the multiple scattering clearly dominates in the energy range of $p = 1\text{GeV}/c$. This makes the multiple scattering fit the better candidate for high granularity pixel detectors at low-momentum experiments and the single helix fit for experiments with a very low radiation length and for very high momenta.

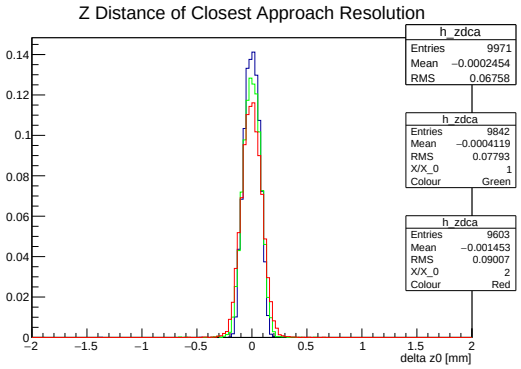

(a) Δz_0 of $p = 1\text{GeV}/c$ muon reconstructed with a multiple scattering fit.

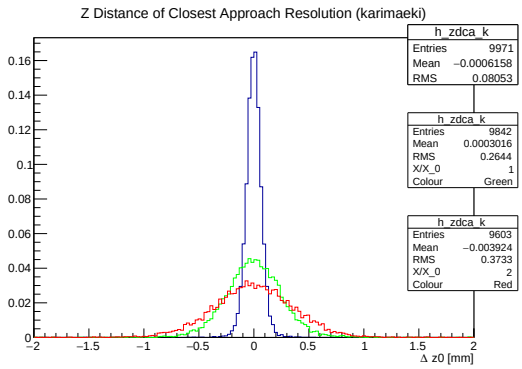

(b) Δz_0 of $p = 1\text{GeV}/c$ muon reconstructed with a single helix fit.

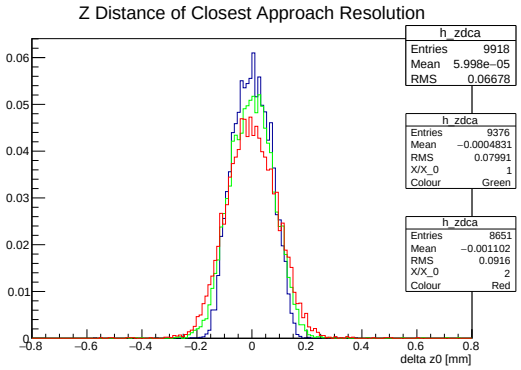

(c) Δz_0 of $p = 1\text{GeV}/c$ electron reconstructed with a multiple scattering fit.

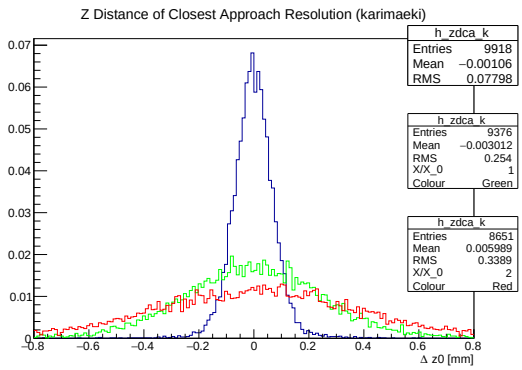

(d) Δz_0 of $p = 1\text{GeV}/c$ electron reconstructed with a single helix fit.

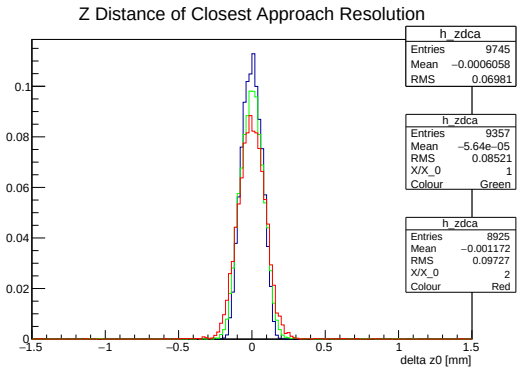

(e) Δz_0 of $p = 1\text{GeV}/c$ pion reconstructed with a multiple scattering fit.

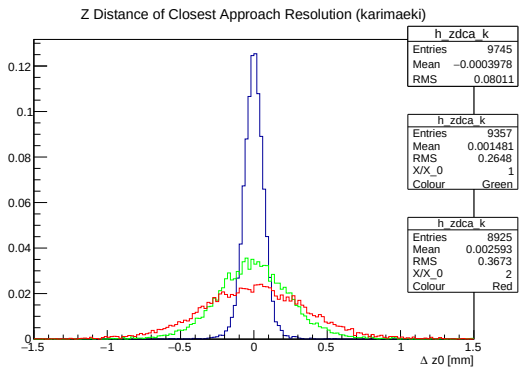

(f) Δz_0 of $p = 1\text{GeV}/c$ pion reconstructed with a single helix fit.

Figure 5.2: Particles are generated at $z_0 = 0$, therefore the resolution is given by the value itself. Figures (a), (c), (e) show the z_0 resolution for generated muons, electrons and pions, respectively, which were obtained by the multiple scattering fit. Similarly for Figures (b), (d), (e), where the single helix fit is used. The distribution for a relative radiation length of $0.1\%X/X_0$ is illustrated in blue, for $1\%X/X_0$ in green and for $2\%X/X_0$ in red.

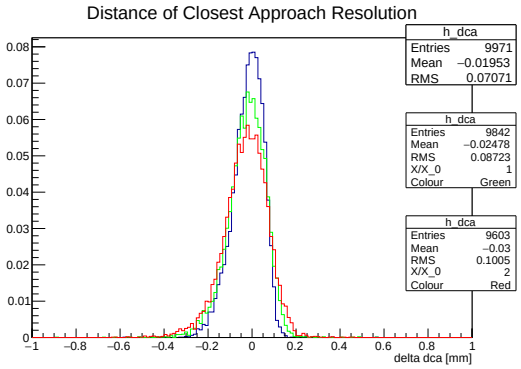

(a) *dca* of $p = 1\text{GeV}/c$ muon reconstructed with a multiple scattering fit.

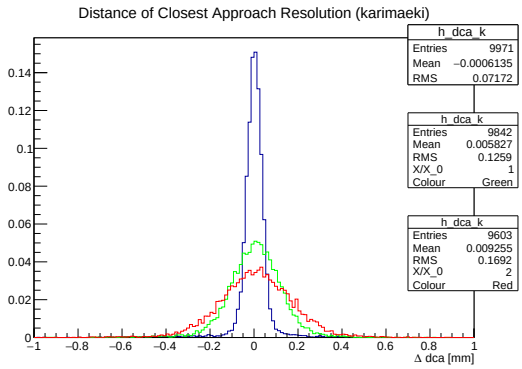

(b) *dca* of $p = 1\text{GeV}/c$ muon reconstructed with a single helix fit.

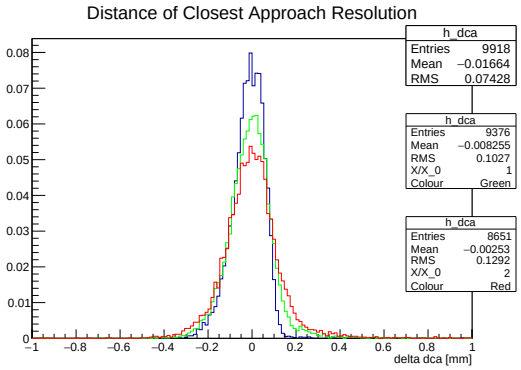

(c) *dca* of $p = 1\text{GeV}/c$ electron reconstructed with a multiple scattering fit.

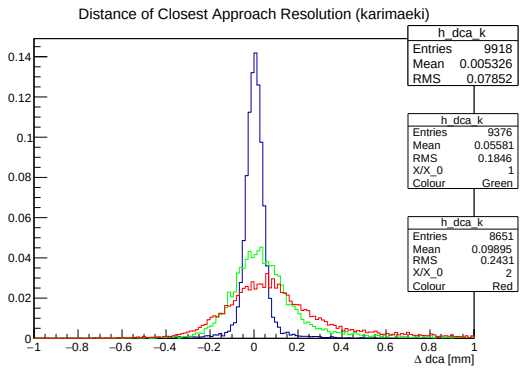

(d) *dca* of $p = 1\text{GeV}/c$ electron reconstructed with a single helix fit.

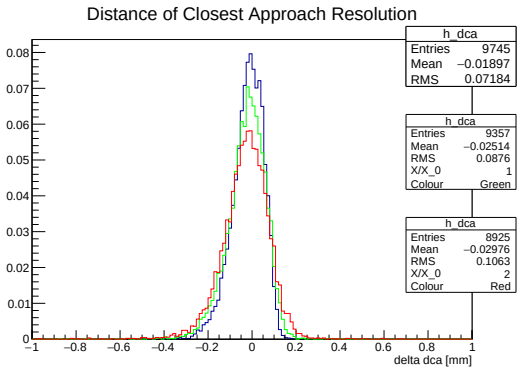

(e) *dca* of $p = 1\text{GeV}/c$ pion reconstructed with a multiple scattering fit.

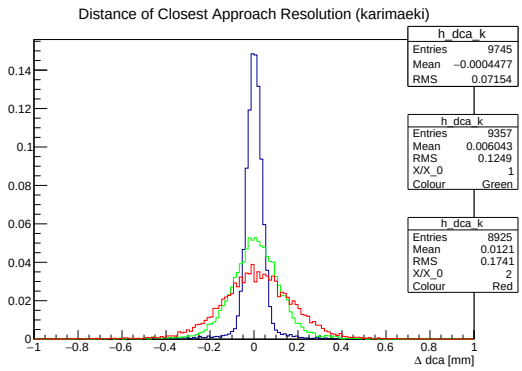

(f) *dca* of $p = 1\text{GeV}/c$ pion reconstructed with a single helix fit.

Figure 5.3: Figures (a), (c), (e) show the *dca* resolution for generated muons, electrons and pions, respectively, which were obtained by the multiple scattering fit. Similarly for Figures (b), (d), (e), where the single helix fit is used. The distribution for a relative radiation length of $0.1\%X/X_0$ is illustrated in blue, for $1\%X/X_0$ in green and for $2\%X/X_0$ in red.

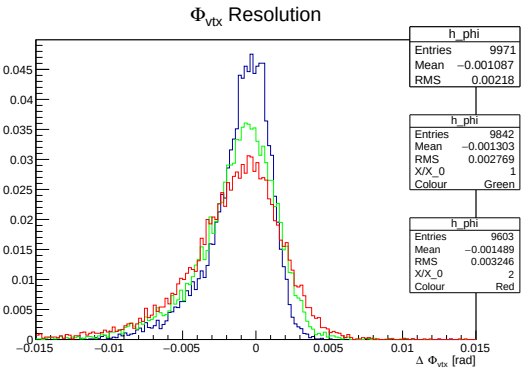

(a) $\Delta\Phi_{vtx}$ of muon at 1GeV, reconstructed with multiple scattering fit.

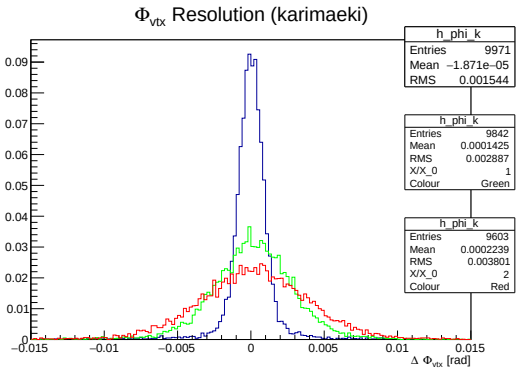

(b) $\Delta\Phi_{vtx}$ of muon at 1GeV, reconstructed with a single helix fit.

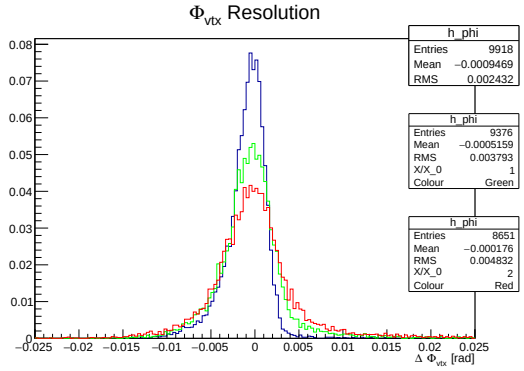

(c) $\Delta\Phi_{vtx}$ of electron at 1GeV, reconstructed with a single multiple scattering fit.

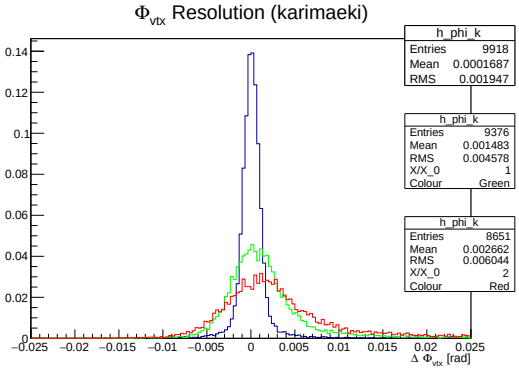

(d) $\Delta\Phi_{vtx}$ of electron at 1GeV, reconstructed with a single helix fit.

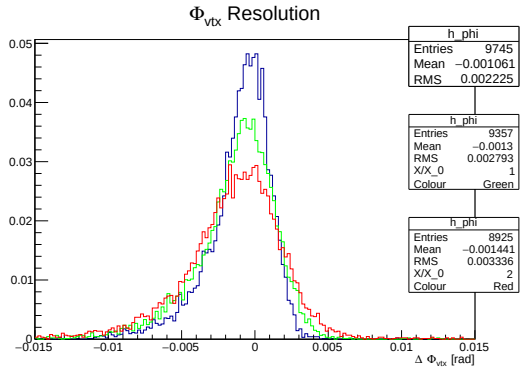

(e) $\Delta\Phi_{vtx}$ of pion at 1GeV, reconstructed with multiple scattering fit.

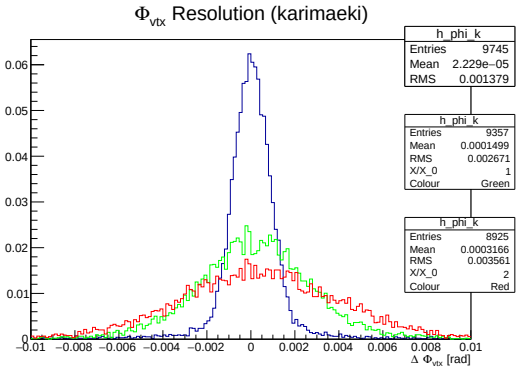

(f) $\Delta\Phi_{vtx}$ of pion at 1GeV, reconstructed with a single helix fit.

Figure 5.4: Figures (a), (c), (e) show the Φ_{vtx}resolution for generated muons, electrons and pions, respectively, which were obtained by the multiple scattering fit. Similarly for Figures (b), (d), (e), where the single helix fit is used. The distribution for a relative radiation length of $0.1\% X/X_0$ is illustrated in blue, for $1\% X/X_0$ in green and for $2\% X/X_0$ in red.

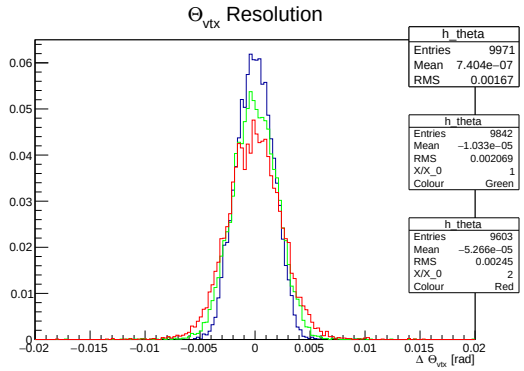

(a) $\Delta\Theta_{vtx}$ of $p = 1\text{GeV}/c$ muon reconstructed with a multiple scattering fit.

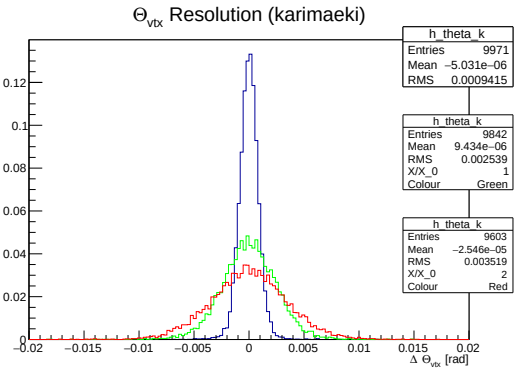

(b) $\Delta\Theta_{vtx}$ of $p = 1\text{GeV}/c$ muon reconstructed with a single helix fit.

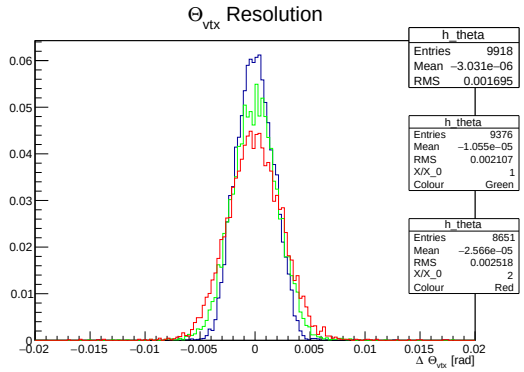

(c) $\Delta\Theta_{vtx}$ of $p = 1\text{GeV}/c$ electron reconstructed with a multiple scattering fit.

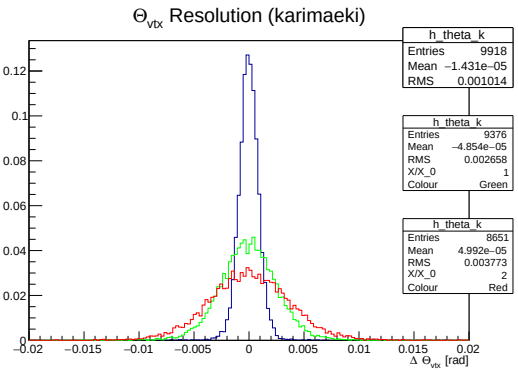

(d) $\Delta\Theta_{vtx}$ of $p = 1\text{GeV}/c$ electron reconstructed with a single helix fit.

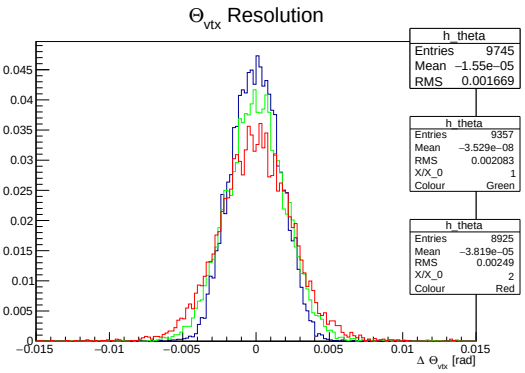

(e) $\Delta\Theta_{vtx}$ of $p = 1\text{GeV}/c$ pion reconstructed with a multiple scattering fit.

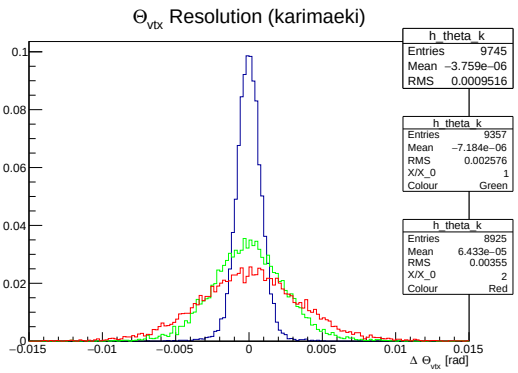

(f) $\Delta\Theta_{vtx}$ of $p = 1\text{GeV}/c$ pion reconstructed with a single helix fit.

Figure 5.5: Figures (a), (c), (e) show the Θ_{vtx} resolution for generated muons, electrons and pions, respectively, which were obtained by the multiple scattering fit. Similarly for Figures (b), (d), (e), where the single helix fit is used. The distribution for a relative radiation length of $0.1\%X/X_0$ is illustrated in blue, for $1\%X/X_0$ in green and for $2\%X/X_0$ in red.

5.2 Parameter Resolutions at High Energies

In this section the track parameter resolutions are presented in the energy range from 10 to 100 GeV. The data points for $p = 1\text{GeV}/c$ are shown as reference. For such high energies the hit uncertainty dominates over the multiple scattering uncertainty. Therefore, in order to consistently compare results obtained with a single fitting algorithm only results of the single helix fit are shown. In this scope the case of $1\%X/X_0$ is investigated since this represents the goal of the proposed detector in terms of material budget. The vertical error bars indicate the quality of the gaussian fit to dermine the RMS.

One can see for the transverse momentum in Figure 5.6 a nearly linear increase of the resolution which is very similar in terms of shape and magnitude for the muon 5.8a and pion 5.8c. The error bars are smaller than the marker size. For electrons also an increase with an approximately linear trend can be seen. Here, however, the datapoints at 10 and 50GeV generated momentum deviate from the line due to statistical fluctuations. The momentum distribution is widely spread and has a width between 3.4% to 3.9%.

Figure 5.7 portrays the RMS of the Θ_{vtx} fit. For this parameter all particles are equally well reconstructed, ranging from 0.0016 radians at a generated momentum of 1GeV below 0.0001 radians at high momenta. The RMS of the Phi_{vtx} fit shown in Figure 5.8 behaves similar for μ^+ and π^+ and is only slightly higher for e^+.

5.2.1 Discussion of Resolutions at High Energies

The relative momentum resolution shows a proportional dependence towards the generated momentum. This is in accordance to the ATLAS inner detector calibration results [23] where a dependence of

$$\frac{\sigma_p}{p} = (4.83 \pm 0.16) \cdot 10^{-4}\text{GeV}^{-1} \cdot p_T, \tag{5.3}$$

was found. In our case a linear fit of the type

$$\frac{\sigma_{p_T}}{p_T} = \alpha + \beta \cdot p, \tag{5.4}$$

yields the parameters α and β which are shown in Table 5.6. The fits are applied above $p = 40\text{GeV}/c$ since below that level multiple scattering affects the RMS which is not considered by the single helix fit.

The results for the linear fit and thus the dependence of the momentum p exceed the results obtained in the inner detector calibration of the ATLAS experiment in the case of μ^+ and π^+. The variation in the electron reconstruction can be seen both in the

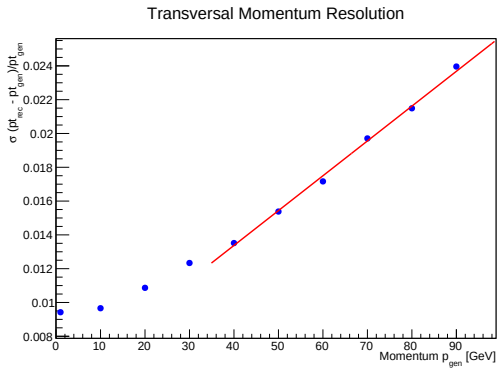

(a) RMS of transverse momentum resolution for μ^+ at high energies.

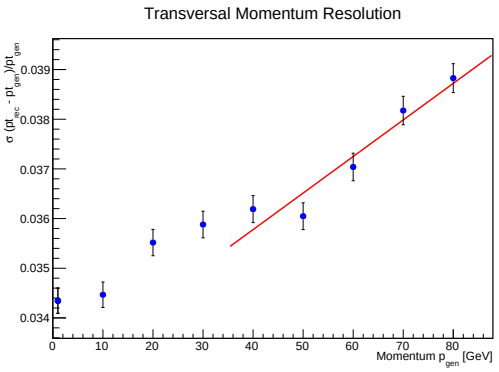

(b) RMS of transverse momentum resolution for e^+ at high energies.

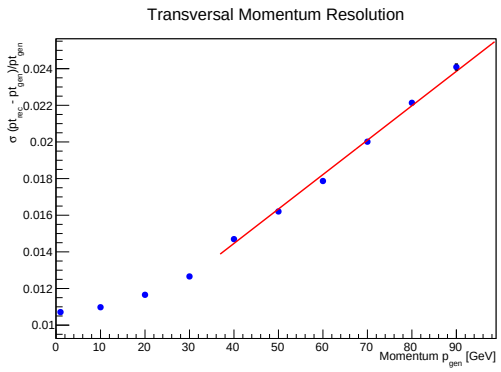

(c) RMS of transverse momentum resolution for π^+ at high energies.

Figure 5.6: Transverse momentum resolutions of the three particles muon (a), electron (b) and pion (c) is illustrated for an energy range of 1 to 100 GeV. The resolution increases linearly at momenta above $p = 40\text{GeV}/c$ where multiple scattering is negligible. A linear fit is applied for this range.

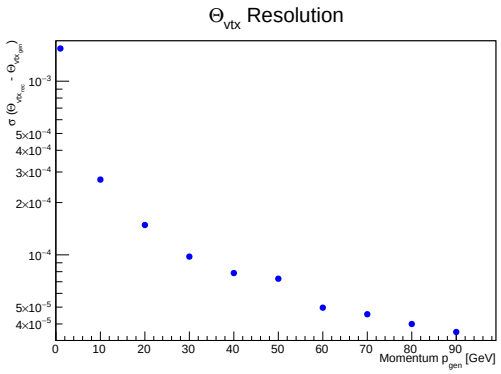

(a) RMS of Θ_{vtx} resolution for μ^+ at high energies.

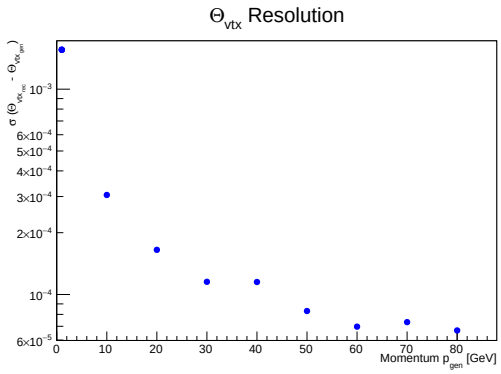

(b) RMS of Θ_{vtx} resolution for e^+ at high energies.

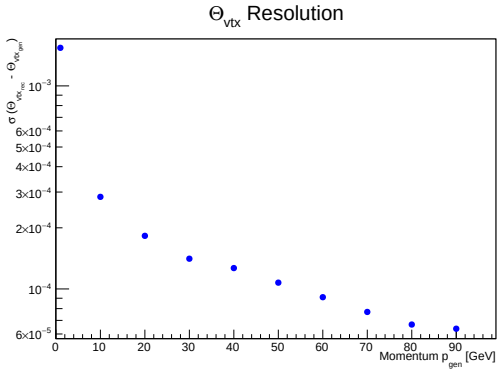

(c) RMS of Θ_{vtx} resolution for π^+ at high energies.

Figure 5.7: Θ_{vtx} resolutions of the three particles muon (a), electron (b) and pion (c) is illustrated for an energy range of 1 to 100 GeV.

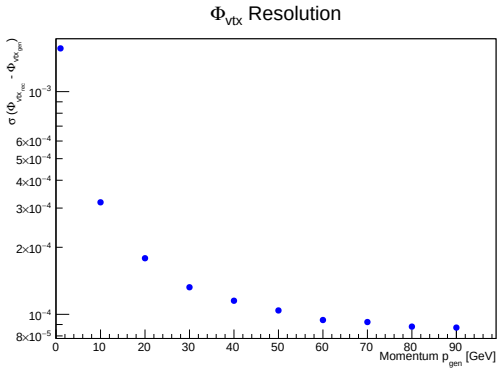

(a) RMS of Φ_{vtx} resolution for μ^+ at high energies.

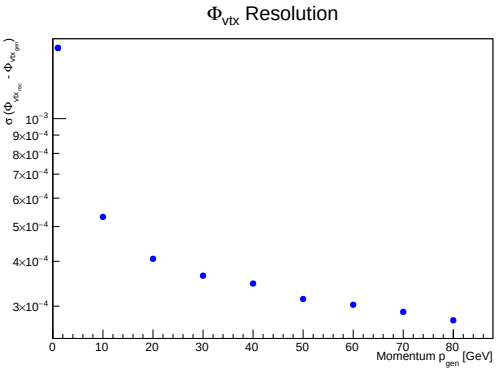

(b) RMS of Φ_{vtx} resolution for e^+ at high energies.

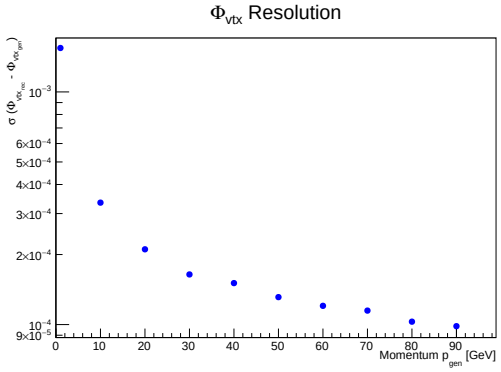

(c) RMS of Φ_{vtx} resolution for pi^+ at high energies.

Figure 5.8: The momentum resolution of the three particle muon (a), electron (b) and pion (c) is illustrated.

Table 5.6: Linear fit results for the relative transverse momentum resolution.

	α	$\beta[\mathrm{GeV}^{-1}]$
μ^+	$(5.1 \pm 0.2) \cdot 10^{-3}$	$(2.06 \pm 0.03) \cdot 10^{-4}$
e^+	$(32.8 \pm 0.5) \cdot 10^{-3}$	$(0.71 \pm 0.09) \cdot 10^{-4}$
π^+	$(6.9 \pm 0.2) \cdot 10^{-3}$	$(1.88 \pm 0.03) \cdot 10^{-4}$

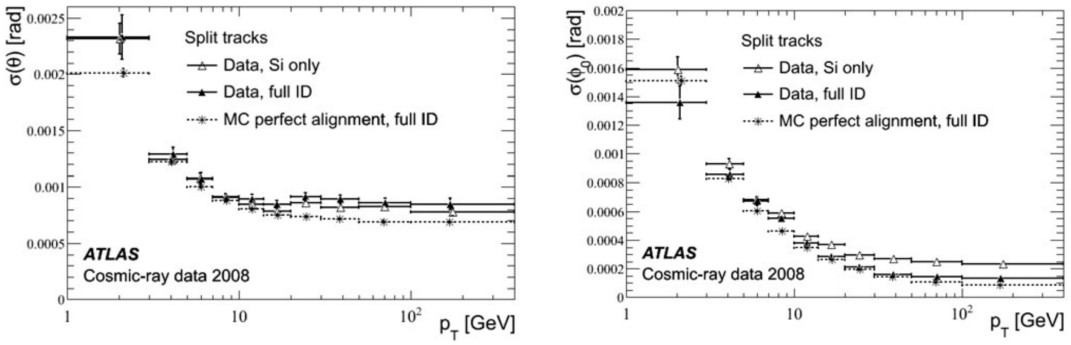

(a) Θ_{vtx} resolution of the ATLAS inner detector calibration.

(b) Φ_{vtx} resolution of the ATLAS inner detector calibration.

Figure 5.9: The results ATLAS inner detector calibration are shown (taken from [23] Fig.21) for a comparison with the results of the triplet9 detector design.

shape and error bars of the graph in Figure 5.6 (b) as well as in the difference of the fit results. They show significantly different behaviour because of the high energy loss due to bremsstrahlung. Also for the resolution of Θ_{vtx} and Φ_{vtx} a comparison can be made to the results of the ATLAS inner detector calibration in [23]. To directly oppose the obtained results Figure 21 of the paper is shown in Figure 5.9. One can see that the resolutions for Φ_{vtx} are almost identical to those of the inner detector calibration and even better for Θ_{vtx}. Of course, one needs to pay attention to the fact that neither the experimental conditions nor the reconstruction methods were the same. The pixel size of the ATLAS inner detector is 50μm (transverse plane)×400μm (longitudinal plane) in comparison to 80μm × 80μm in our case, which explains our better Θ_{vtx} resolution. But even though the pixel size is smaller for ATLAS in the transverse plane, the Φ_{vtx} resolution is similar to our results. This marks an advantage for the *triplet9* design.

The fit used in the ATLAS study takes multiple scattering into account. Because of these differences, no absolute conclusion can be drawn which of the detectors is better in terms of track parameter resolution. However, again, the compliance of the results of the two resolution studies is promising.

5.3 Trigger Application

Only the outer detector triplet is studied here for the trigger application. As explained in Chapter 4 this design is capable of forming trigger decisions depending on the position of the middle hit, and the slope of first and third hit. If the hit at the middle layer lies within a window which is defined around the interaction of a straight line between first and third hit and the middle layer the track is reconstructed and the momentum can be calculated using the beamline constraint.

The difference between the intersection point and the middle hit is illustrated in Figure 5.10 for μ^+, e^+ and π^+ respectively. The histogram on the left shows the differences for the longitudinal plane Δz and the one on the right for the transverse plane $\Delta\Phi_T$:

$$\Delta z = \left| \frac{z_1 + z_3}{2} - z_2 \right|. \tag{5.5}$$

$$\Delta\Phi_T = \left| \frac{\Phi_1 + \Phi_3}{2} - \Phi_2 \right|. \tag{5.6}$$

As one can see in Figure 5.10 the distribution is discrete especially in the case of the ΔZ distributions. This reflects the size of the pixels of $80\mu\text{m} \times 80\mu\text{m}$. Consequently, the difference of the peaks is half of that length. Furthermore, one can confidentially define a Z-window from the plots for this pixel size of $\Delta Z_{max} = 0.1\text{mm}$. This would accept the great majority of particle tracks. The size of the $\Delta\Phi$-cut depends on one wants to allow tracks with lower momenta or not. As the distribution for $\Delta\Phi$ in case of the electron shows (see Figure 5.10 (c),(d)) a cut of 2mrad would allow most electron tracks to be reconstructed, whereas a cut of 1mrad is sufficient to include muon-like or pion-like particles at 1GeV for the pixel-size used in the simulation.

A global cut-criterion can and should not be given but rather the functionality of the trigger application is demonstrated. Determining the window would also require a further study of the fakerate which comes with a certain window in order to find the optimal triggernorm.

Table 5.7: Summary of the $\Delta p_{T,rel}$ values illustrated in Figure 5.1 obtained only using the outermost detector triplet and beamline constraint.

RMS($\Delta p_{T,rel}$)		MS-Fit			Helix-Fit	
particle	$0.1\%X/X_0$	$1\%X/X_0$	$2\%X/X_0$	$0.1\%X/X_0$	$1\%X/X_0$	$2\%X/X_0$
μ^+	0.0057	0.0085	0.0105	0.0044	0.0077	0.0102
e^+	0.0212	0.0458	0.0578	0.0199	0.0698	0.0923
π^+	0.0066	0.0093	0.0119	0.0055	0.0086	0.0115

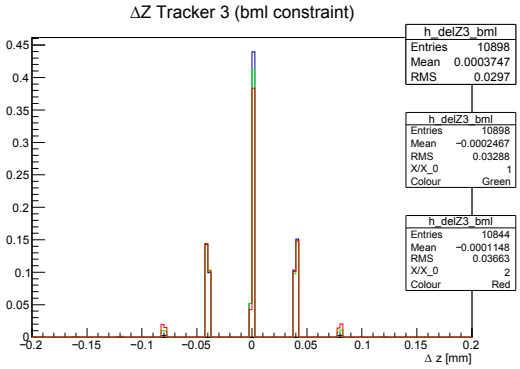

(a) $\Delta\Theta_{vtx}$ of $p = 1\text{GeV}/c$ muon reconstructed with a multiple scattering fit.

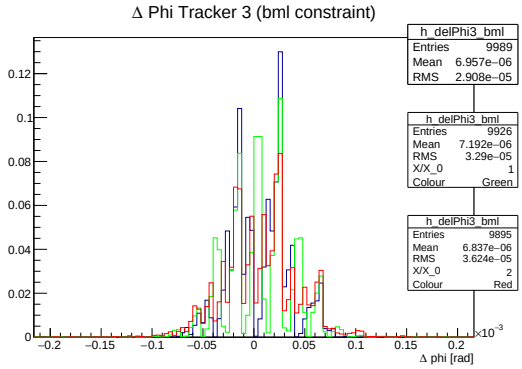

(b) $\Delta\Theta_{vtx}$ of $p = 1\text{GeV}/c$ muon reconstructed with a single helix fit.

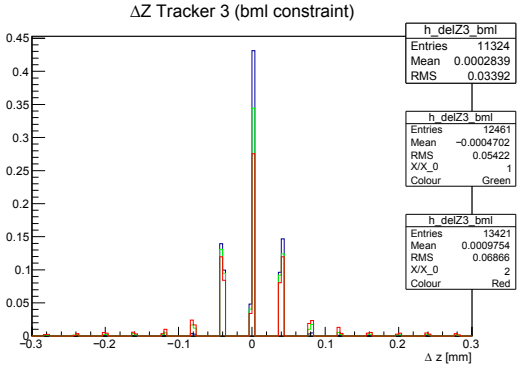

(c) $\Delta\Theta_{vtx}$ of $p = 1\text{GeV}/c$ electron reconstructed with a multiple scattering fit.

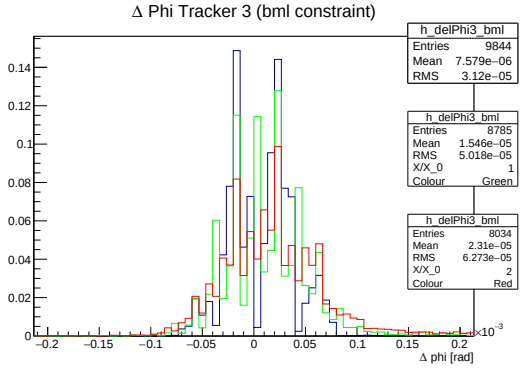

(d) $\Delta\Theta_{vtx}$ of $p = 1\text{GeV}/c$ electron reconstructed with a single helix fit.

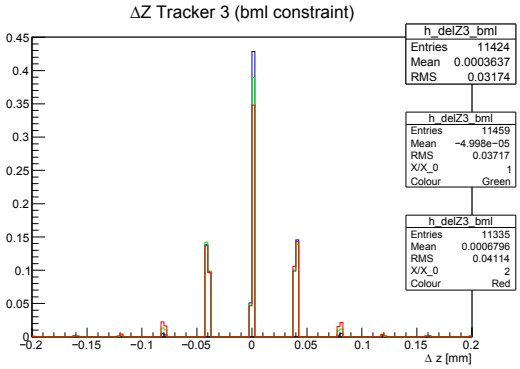

(e) $\Delta\Theta_{vtx}$ of $p = 1\text{GeV}/c$ pion reconstructed with a multiple scattering fit.

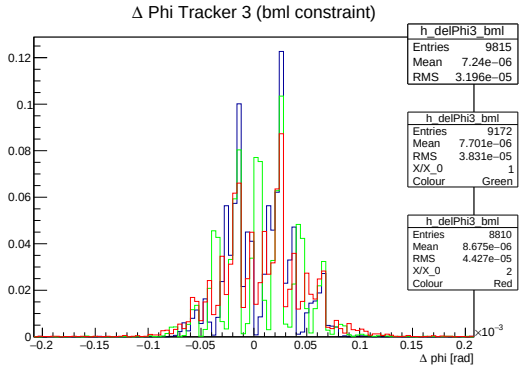

(f) $\Delta\Theta_{vtx}$ of $p = 1\text{GeV}/c$ pion reconstructed with a single helix fit.

Figure 5.10: The differences of the middle hit to the straight line of the other two hits is shown in the longitudinal plane (left) and transverse plane (right) for generated muons, electrons and pions respectively in that order from top to bottom, generated with a momentum of 1GeV.

Figure 5.7 shows the reconstructed relative transverse momentum using only the three outermost layers and beamline constraint which are summarised in Table 5.7. The resolutions for the relative transverse momentum are slightly better then the results for the *triplet9* detector. This is due to the beamline constraint which increases the bending arm. One can draw two conclusions from that fact. Firstly, a beamline constraint would even more enhance the resolution of the full detector and secondly, the reconstruction of $\Delta p_{T,rel}$ functions as expected. Therefore, the outermost detector triplet can be used for Δp_T reconstruction in a trigger application.

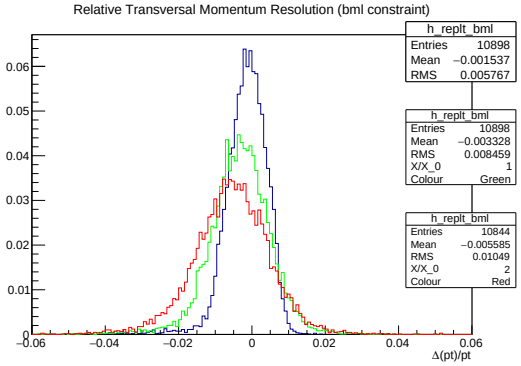

(a) $p_{T,rel}$ of $p = 1\text{GeV}/c$ muon reconstructed with a multiple scattering fit.

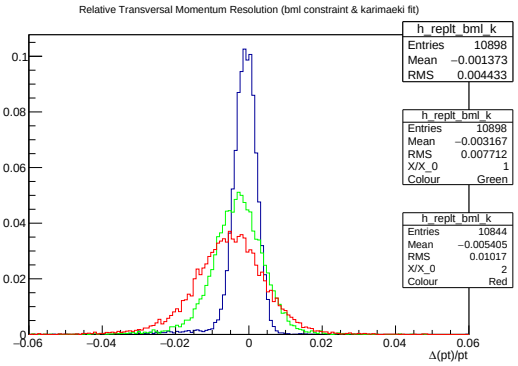

(b) $p_{T,rel}$ of $p = 1\text{GeV}/c$ muon reconstructed with a single helix fit.

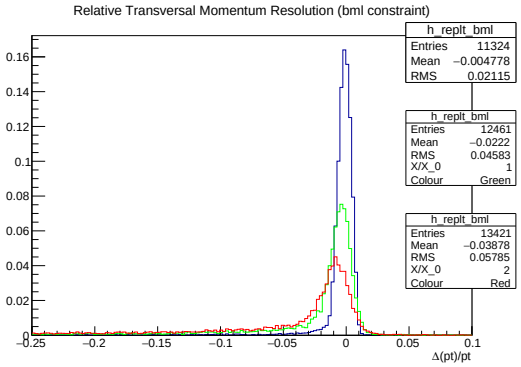

(c) $p_{T,rel}$ of $p = 1\text{GeV}/c$ electron, reconstructed with a multiple scattering fit.

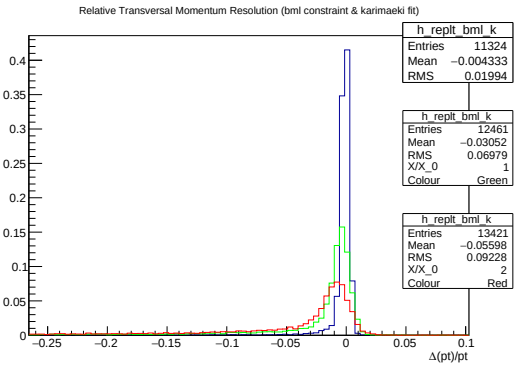

(d) $p_{T,rel}$ of $p = 1\text{GeV}/c$ electron reconstructed with a single helix fit.

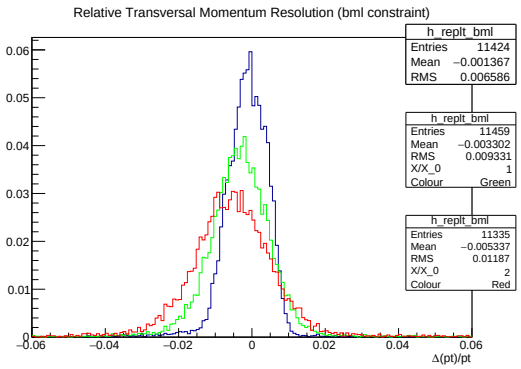

(e) $p_{T,rel}$ of $p = 1\text{GeV}/c$ pion reconstructed with a multiple scattering fit.

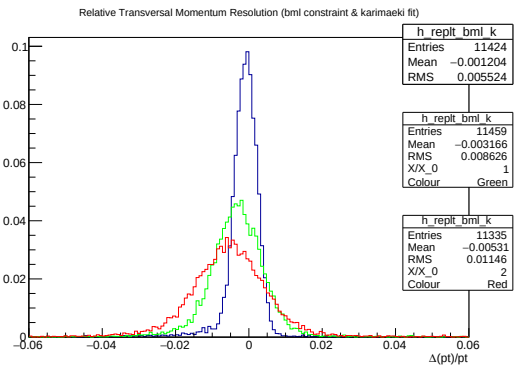

(f) $p_{T,rel}$ of $p = 1\text{GeV}/c$ pion reconstructed with a single helix fit.

Figure 5.11: Figures (a), (c), (e) show the $p_{T,rel}$ resolution for generated muons, electrons and pions, respectively, which were obtained by the multiple scattering fit. Similarly for Figures (b), (d), (e), where the single helix fit is used. The distribution for a relative radiation length of $0.1\%X/X_0$ is illustrated in blue, for $1\%X/X_0$ in green and for $2\%X/X_0$ in red. Only the three hits of the outer detector triplet and beamline constraint were used.

6 Conclusion

The thesis first motivates the concept of an all-pixel tracking detector by arguing, that number of layers and overall complexity of an all-purpose detector can be highly reduced. The *triplet9* design, consisting of three groups of each three closely stacked pixel layers, is presented.

It is explained how the three investigated material compositions of 0.1%, 1% and 2% of radiation length were obtained with regard to the implied assumptions and approximations in the simulation. Furthermore, the concept of hit triplets is introduced together with their benefits for track reconstruction and the correlation of hit triplets to the detector layout is emphasised. The track reconstruction algorithm and the two fit methods used for this purpose are described accordingly: the Triplet Fit [21] to account for multiple scattering and the Single Helix Fit [22] to address hit uncertainties.

Moreover, the possible application of the detector design for a track trigger by using only the outermost detector layer triplet (*triplet3 design*) and its working principle is pointed out.

Finally, the results for the track parameter reconstruction are presented for μ^+, e^+ and π^+ with momentum $p = 1\text{GeV}/c$. The effects of different radiation lengths is perceived by a broadening of the resolution of the reconstructed parameters. The resolutions for μ^+ and π^+ are very similar to each other which shows that hadronic interactions for π^+ are negligible. The track parameter resolution for e^+ shows the expected tails resulting from bremsstrahlung. The reconstruction performance of the triplet fit was overall better then the single helix fit except for 0.1% radiation length where multiple scattering is not the dominant source of measurement uncertainties.

In addition, the dependence of the resolution on the particle momenta is displayed for simulated μ^+, e^+, π^+ with a relative radiation length of the detector layers of $1\%X/X_0$. The single helix fit is used since hit uncertainties are dominant for high energies up to 100 GeV. Even though the fit does not account for multiple scattering, better resolutions are obtained than in the ATLAS inner detector calibration measurement [23]. This is remarkable since the pixel size used in the ATLAS pixel detector is $50\mu\text{m} \times 400\mu\text{m}$ [24] thus smaller in the transverse plane.

Finally, the trigger application of the *triplet3* design is successfully demonstrated. Cut criteria are derived which can be used to trigger for secondary particles or to

determine whether particles originate from the same vertex. The resolution of the transverse momentum using only the outermost detector triplet and beamline constraint matches the requirements to apply cuts in the slope ϕ' (see Equation **??**) relative to the vertex to reject secondary particles and to reduce pileup.

6.1 Outlook

The results obtained for the studied *triplet9* detector design are promising. The special detector layout allows track reconstruction of very high precision. A resolution for $\sigma(p_T)/p$, Θ_{vtx} and Φ_{vtx} is achieved that at least matches or even exceeds LHC standards.

Furthermore, the demonstrated advantage of the design to function as a track trigger extends the application area of the detector. It further provides the possibility to function as a completely independent element with the *triplet3* design, consisting of only the three outermost layers.

Therefore, the conclusion can be drawn that a pixel-only detector and in particular a design consisting of closely stacked triple layers, represents a very good alternative for the upcoming LHC upgrade or future experiments conducted at the Future Circular Collider in order to cope with the next stage of high-energy and high-luminosity experiments.

List of Figures

Bibliography

[1] ATLAS. http://atlas.ch/inner_detector1.html.

[2] Geant4. http://geant4.web.cern.ch/geant4/UserDocumentation/UsersGuides/PhysicsReferenceManual/fo/PhysicsReferenceManual.pdf, Dec 2014.

[3] K.A. Olive et al. (Particle Data Group). Passage of particles through matter. *Chin. Phys.*, C, 38, 090001, 2014.

[4] H. Bethe and W. Heitler. On the stopping of fast particles and on the creation of positive electrons. *Proceedings of the Royal Society of London A: Mathematical, Physical and Engineering Sciences*, 146(856):83–112, 1934.

[5] E. Rutherford. Lxxix. the scattering of α and β particles by matter and the structure of the atom. *Philosophical Magazine Series 6*, 21(125):669–688, 1911.

[6] S. Goudsmit and J. L. Saunderson. Multiple scattering of electrons. *Phys. Rev.*, 57:24–29, Jan 1940.

[7] H. W. Lewis. Multiple scattering in an infinite medium. *Phys. Rev.*, 78:526–529, Jun 1950.

[8] Virgil L. Highland. Some practical remarks on multiple scattering. *Nuclear Instruments and Methods*, 129(2):497 – 499, 1975.

[9] Gerald R. Lynch and Orin I. Dahl. Approximations to multiple coulomb scattering. *Nuclear Instruments and Methods in Physics Research Section B: Beam Interactions with Materials and Atoms*, 58(1):6 – 10, 1991.

[10] Yung-Su Tsai. Pair production and bremsstrahlung of charged leptons. *Rev. Mod. Phys.*, 46:815–851, Oct 1974.

[11] K.A. Olive et al. (Particle Data Group). Atomic and nuclear properties of materials. *Chin. Phys.*, C, 38, 090001, 2014.

[12] S. Tavenir. *Experimental Techniques in Nuclear and Particle Physics*. Springer, 2010.

[13] A. Blondel, A. Bravar, M. Pohl, S. Bachmann, N. Berger, et al. Research Proposal for an Experiment to Search for the Decay $\mu \to eee$. 2013.

[14] I. Perić, C. Kreidl, and P. Fischer. Particle pixel detectors in high-voltage {CMOS} technology—new achievements. *Nuclear Instruments and Methods in Physics Research Section A: Accelerators, Spectrometers, Detectors and Associated Equipment*, 650(1):158 – 162, 2011. International Workshop on Semiconductor Pixel Detectors for Particles and Imaging 2010.

[15] I Peric. Active pixel sensors in high-voltage cmos technologies for atlas. *Journal of Instrumentation*, 7(08):C08002, 2012.

[16] A Schöning. Three-dimensional triplet tracking for lhc and future high rate experiments. *Journal of Instrumentation*, 9(10):C10025, 2014.

[17] K.A. Olive et al. (Particle Data Group). 42. monte carlo particle numbering scheme. *Chin. Phys.*, C, 38, 090001, 2014.

[18] R. E. Kalman. A New Approach to Linear Filtering and Prediction Problems. *Transactions of the ASME – Journal of Basic Engineering*, (82 (Series D)):35–45, 1960.

[19] Claus Kleinwort. General broken lines as advanced track fitting method. *Nuclear Instruments and Methods in Physics Research Section A: Accelerators, Spectrometers, Detectors and Associated Equipment*, 673(0):107 – 110, 2012.

[20] Moritz Kiehn. A fast and parallel three-dimensional track fit with multiple scattering for mu3e, 02 2015.

[21] A Schöning. A three-dimensional helix fit with multiple scattering using hit triplets. *publication in preparation.*

[22] V Karimäki. Effective circle fitting for particle trajectories. pages 187–191, 1991.

[23] ATLAS Collaboration. The atlas inner detector commissioning and calibration. *The European Physical Journal C*, 70(3):787–821, 2010.

[24] Fabian Huegging (for the ATLAS Pixel collaboration). The ATLAS Pixel Detector. IEEE Trans.Nucl.Sci. 53 (2006) 1732-1736, 2004. arXiv:physics/0412138v2.

Danksagung

An dieser Stelle möchte ich mich bei all jenen bedanken, die mir bei der Umsetzung und Gestaltung dieser Arbeit geholfen haben.

Als erstes bedanke ich mich bei Herrn Prof. Dr. André Schöning, nicht nur für die Anregung zu diesem spannenden Thema, sondern auch dafür mir jederzeit bei Problemen und Fragen zur Seite zu stehen.

Mein Dank gilt auch Herrn Prof. Dr. Schultz-Coulon für seine Bereitschaft und sein Interesse sich mit dem Thema dieser Arbeit außeinanderzusetzen.

Außerdem bedanke ich mich bei Moritz Kiehn und Alexandr Kozlinskiy für die vielen Erklärungen und Hilfestellungen.

Nicht zuletzt danke ich auch meiner Familie und Tania Christiansen für die vielseitige Unterstützung, die über diese Arbeit hinausgeht.

Erklärung

Ich versichere, dass ich diese Arbeit selbstständig verfasst und keine anderen als die angegebenen Quellen und Hilfsmittel benutzt habe.

Heidelberg, den 20.03.2015